Comput Geosci
DOI 10.1007/s10596-007-9070-x

ORIGINAL PAPER

A locally conservative variational multiscale method for the simulation of porous media flow with multiscale source terms

Ruben Juanes · Francois-Xavier Dub

Received: 3 August 2006 / Accepted: 16 October 2007

Abstract We present a variational multiscale mixed finite element method for the solution of Darcy flow in porous media, in which both the permeability field and the source term display a multiscale character. The formulation is based on a multiscale split of the solution into coarse and subgrid scales. This decomposition is invoked in a variational setting that leads to a rigorous definition of a (global) coarse problem and a set of (local) subgrid problems. One of the key issues for the success of the method is the proper definition of the boundary conditions for the localization of the subgrid problems. We identify a weak compatibility condition that allows for subgrid communication across element interfaces, a feature that turns out to be essential for obtaining high-quality solutions. We also remove the singularities due to concentrated sources from the coarse-scale problem by introducing additional multiscale basis functions, based on a decomposition of fine-scale source terms into coarse and deviatoric components. The method is locally conservative and employs a low-order approximation of pressure and velocity at both scales. We illustrate the performance of the method on several synthetic cases and conclude that the method is able to capture the global and local flow patterns accurately.

R. Juanes (✉) · F.-X. Dub
Massachusetts Institute of Technology,
77 Massachusetts Ave, Bldg 48, Cambridge,
MA 02139, USA
e-mail: juanes@mit.edu

Keywords Porous media · Pressure equation · Heterogeneity · Local mass conservation · Variational multiscale · Mixed finite element method

1 Introduction

The equations governing the flow of fluids in the subsurface (oil and gas reservoirs, confined aquifers, vadose zone, etc.) can, in many cases, be formulated in terms of a single "pressure" equation (of elliptic character) describing an overall mass balance and "component" equations (of hyperbolic character) governing the differential displacement of each component [8].

In this work, we concentrate on the numerical solution of a model pressure equation:

$$\nabla \cdot (-\mathsf{k}\nabla p) = f, \tag{1}$$

where the coefficient tensor k is discontinuous, highly variable, and may present short and long correlation lengths. Moreover, the source/sink term f displays a multiscale character also. In practical scenarios, flow is driven by injection and production wells. Because wells are features that are much smaller than the grid size, they must be understood as concentrated (point or line) sources.

A number of approaches are currently being investigated for the numerical simulation of porous media flow with rough permeability fields. We can identify at least two main tracks: multiscale finite element or finite volume methods, and variational multiscale (VMS) methods.

The multiscale finite element method was originally proposed in [20] for the solution of elliptic equations

with rapidly oscillating coefficients. The main idea is to construct finite element basis functions that themselves are solutions to the elliptic operator inside each element and, therefore, capture small scale information [10, 11]. The method was analyzed in a series of subsequent papers (see, e.g., [19, 21]). A mixed finite element version that guarantees local mass conservation at the element level was proposed in [16]. This work was recently extended in a number of important ways by the Norwegian school [1, 2]. Inspired in the multiscale finite element method, a multiscale finite volume method was proposed in [24]. This method also preserves mass conservation at the coarse and fine scales (see also [25, 28]).

The VMS method was originally proposed by Hughes et al. [22, 23] as an overarching framework for the solution of partial differential equations that exhibit multiscale phenomena (either due to small-scale heterogeneity or sharp features that cannot be captured on a coarse grid). The essence of the method is to perform a multiscale split of the solution into a coarse-scale part (that can be approximated on a coarse grid) and a subscale component. The multiscale split is invoked in a variational setting, which leads to a rigorous definition of a coarse-scale problem and a subgrid-scale problem. Although an approximation (localization) of the subgrid problem is typically necessary, the framework offers a rigorous formulation for incorporating subgrid effects in the coarse scale equations. A mixed variant of the method, coined "numerical subgrid upscaling," was developed independently by Arbogast et al. [3–5, 7].

Links between the mixed version of the VMS approach and the mixed multiscale finite element method have been pointed out recently [6]. A thorough comparison of the different multiscale methods (as well as interesting extensions) has recently been presented in [27].

In the present paper, we adopt the VMS framework to develop a locally conservative multiscale method. We extend the formulation presented in [26] to account for the presence of source terms with a multiscale character (wells). The main contributions are:

1. We propose an enhanced *localization assumption* needed to define the local subgrid problems, which allows for subgrid communication across element interfaces and boundaries.
2. We introduce multiscale "well" basis functions, based on a decomposition of fine-scale source terms into coarse and deviatoric components.

One of the main features of the proposed method is the relaxed localization assumption with respect to the numerical subgrid upscaling method [4]. We do not provide direct numerical comparisons between the two methods, for two reasons. First, results in [4] use a higher-order velocity space (BDM_1) on the coarse scale, whereas we use the lowest-order space (RT_0)—therefore, a fair direct comparison is difficult. We point out, however, that the choice of RT_0 in the numerical subgrid upscaling method would imply that the subscales are identically equal to zero—clearly a limitation. Second, in the paper, we show that, *in the absence of multiscale source terms*, our method is equivalent to a multiscale mixed finite element method [2]. A thorough comparison of different multiscale techniques (including the numerical subgrid upscaling method) is provided by [27].

The proposed approach to handle concentrated sources is fundamentally different from the one proposed in [34]. Both approaches superpose two solutions: a well solution and a background solution. The split in [34] is succinctly expressed in a paragraph from their paper: "...the source term is removed from the coarse cell that contains the well; the well effects, which are captured by the well basis function, are represented on the coarse scale as integral contributions to adjacent coarse cells." In contrast, our background solution contains the entire strength of the source term, albeit averaged (constant over the well gridblock). The well contribution (more generally, the contribution from any multiscale source term) is the solution to a local problem with zero integral divergence—purely a deviatoric (or zero-mean) source term. Our treatment effectively removes the well singularity from the coarse-scale problem, is naturally mass conservative, and allows well regions to overlap.

In Section 2, we introduce the governing equations and the mixed finite element approximation of the global fine-scale problem. The VMS mixed finite element method is developed in Section 3, with special emphasis on the enhanced localization assumption we propose. In Section 4, we extend the method to incorporate multiscale source terms. In Section 5, we illustrate the performance of the proposed method on a number of challenging simulations. Finally, in Section 6, we draw the main conclusions of this investigation.

2 Mathematical formulation

2.1 Governing equations

We shall use the following model pressure equation:

$$\nabla \cdot \mathbf{u} = f \quad \text{in } \Omega, \tag{2}$$

where f is the source term, which may be highly variable and display a multiscale character, and $\mathbf{u}$ is the total velocity given by Darcy's law:

$$\mathbf{u} = -\mathsf{k}\nabla p. \tag{3}$$

The symbol k is the permeability tensor, and p is the pressure. In a more general setting (multiphase flow problems including gravity effects), k is the total mobility tensor, and p is the flow potential. The permeability tensor is symmetric and positive definite. The components of k are assumed to be bounded, but they may be highly discontinuous and display large anisotropy ratios. In this work, we shall assume that k is a diagonal tensor. The pressure equation is supplemented with the following boundary conditions:

$$p = \bar{p} \quad \text{on } \Gamma_p, \tag{4}$$

$$\mathbf{u}\cdot\mathbf{n} = \bar{u} \quad \text{on } \Gamma_u, \tag{5}$$

where $\Gamma_p \cap \Gamma_u = \emptyset$, $\Gamma_p \cup \Gamma_u = \partial\Omega$, and n is the outward unit normal to the boundary. For expositional simplicity and without loss of generality (see, e.g., Section IV.1 of [13]), we may take a homogeneous Neumann boundary condition:

$$\bar{u} = 0 \quad \text{on } \Gamma_u. \tag{6}$$

2.2 Mixed variational formulation

We write Eqs. 2 and 3 in the following form:

$$\mathsf{k}^{-1}\mathbf{u} + \nabla p = 0, \tag{7}$$

$$\nabla\cdot\mathbf{u} = f. \tag{8}$$

We introduce the following functional spaces:

$$W \equiv L^2(\Omega) = \left\{ q : \int_\Omega |q|^2 \,\mathrm{d}\Omega = \|q\|^2_{L^2(\Omega)} < +\infty \right\}, \tag{9}$$

with inner product

$$(q, p) := \int_\Omega q\, p \,\mathrm{d}\Omega, \quad q, p \in L^2(\Omega), \tag{10}$$

and

$$H(\mathrm{div}, \Omega) = \left\{ \mathbf{v} : \mathbf{v} \in (L^2(\Omega))^2, \nabla\cdot\mathbf{v} \in L^2(\Omega) \right\}, \tag{11}$$

with inner product

$$(\mathbf{v}, \mathbf{u}) := \int_\Omega \mathbf{v}\cdot\mathbf{u} \,\mathrm{d}\Omega, \quad \mathbf{v}, \mathbf{u} \in H(\mathrm{div}, \Omega). \tag{12}$$

The space $L^2(\Omega)$ is the usual Sobolev space of square integrable functions in Ω. The space $H(\mathrm{div}, \Omega)$ is defined such that a vector $\mathbf{v}$ belonging to this space admits a well-defined normal trace on $\partial\Omega$ [13, Section III.1.1]:

$$\bar{v} \equiv \mathbf{v}\cdot\mathbf{n} \in H^{-1/2}(\partial\Omega). \tag{13}$$

We will also make use of the following space:

$$V \equiv H_{0,u}(\mathrm{div}, \Omega) = \{ \mathbf{v} : \mathbf{v} \in H(\mathrm{div}, \Omega), \mathbf{v}\cdot\mathbf{n} = 0 \text{ on } \Gamma_u \}. \tag{14}$$

of functions in $H(\mathrm{div}, \Omega)$ with null normal trace on the Neumann boundary Γ_u. Denoting by $H^{1/2}(\Gamma)$ the dual space of $H^{-1/2}(\Gamma)$ for $\Gamma \subset \partial\Omega$, we also define the duality product:

$$\langle \bar{u}, \bar{p} \rangle_\Gamma := \int_\Gamma \bar{u}\bar{p} \,\mathrm{d}\Gamma, \quad \bar{u} \in H^{-1/2}(\Gamma), \ \bar{p} \in H^{1/2}(\Gamma). \tag{15}$$

Making use of the functional spaces defined above, we can express the problem given by Eqs. 7 and 8 with boundary conditions (4)–(6) in mixed variational form: Find $(\mathbf{u}, p) \in V \times W$ such that

$$(\mathbf{v}, \mathsf{k}^{-1}\mathbf{u}) - (\nabla\cdot\mathbf{v}, p) = -\langle \mathbf{v}\cdot\mathbf{n}, \bar{p} \rangle_{\Gamma_p} \quad \forall \mathbf{v} \in V, \tag{16}$$

$$(w, \nabla\cdot\mathbf{u}) = (w, f) \quad \forall w \in W. \tag{17}$$

It is well known that this problem has a unique solution [13].

2.3 The mixed finite element method

The mixed variational formulation provides the basis for the mixed finite element method. Let $V_h \subset V$ and $W_h \subset W$ be finite dimensional subspaces of the corresponding continuum spaces, the mixed finite element approximation of Eqs. 16 and 17 reads: Find $(\mathbf{u}_h, p_h) \in V_h \times W_h$ such that

$$(\mathbf{v}_h, \mathsf{k}^{-1}\mathbf{u}_h) - (\nabla\cdot\mathbf{v}_h, p_h) = -\langle \mathbf{v}_h\cdot\mathbf{n}, \bar{p} \rangle_{\Gamma_p} \quad \forall \mathbf{v}_h \in V_h, \tag{18}$$

$$(w_h, \nabla\cdot\mathbf{u}_h) = (w_h, f) \quad \forall w_h \in W_h. \tag{19}$$

The spaces V_h and W_h cannot be chosen independently; they must satisfy a standard coercivity condition and the discrete inf-sup condition [9, 12]. The numerical solution of Eqs. 18 and 19 invariably involves a partition $\mathscr{T}_h$ of the domain Ω into nonoverlapping elements e_i, $\mathscr{T}_h = \bigcup_{i=1}^{N_h} e_i$, where N_h is the number of elements of the grid. We also define the skeleton of the partition, $\mathscr{S}_h = \bigcup_{a=1}^{M_h} \gamma_a$, where M_h is the number of element faces denoted by γ_a. We shall understand the partition $\mathscr{T}_h$ as the fine grid, on which the permeability k is defined. For definiteness, we shall use a partition

into rectangular elements and associate the fine-scale velocity space with the lowest-order Raviart–Thomas space, $RT_0(\mathscr{T}_h)$ [31]:

$$V_h = \left\{ \mathbf{v}_h : \mathbf{v}_h = \sum_{a=1}^{M_h} \mathbf{N}_a^h \mathsf{v}_a, \quad \mathsf{v}_b = 0 \; \forall \gamma_b \in \Gamma_u \right\}, \tag{20}$$

where $\mathbf{N}_a^h$ is the RT_0 basis function associated with face γ_a and v_a is the corresponding degree of freedom (the integrated flux through face γ_a). The corresponding pressure approximation is piecewise constant on the fine mesh, $P_0(\mathscr{T}_h)$:

$$W_h = \left\{ w_h : w_h = \sum_{i=1}^{N_h} \chi_i^h \mathsf{w}_i \right\}, \tag{21}$$

where χ_i^h is the characteristic function for element i (equal to one at element e_i, zero at all other elements) and w_i is the corresponding degree of freedom (the average pressure at element e_i).

Other choices of velocity and pressure spaces are of course possible [13]. The RT_0 space is, however, the simplest. Moreover, it can be shown that, for diagonal permeability tensor and under appropriate numerical quadrature, this method reduces to the traditional finite difference method [32, 33].

3 The variational multiscale method

3.1 Principle

The essence of the VMS method [22, 23] is to perform a multiscale split of the solution into a coarse-scale part (that can be approximated on a coarse grid) and a subscale component. The multiscale split is invoked in a variational setting, which leads to a rigorous definition of a coarse-scale problem and a subgrid-scale problem. By virtue of this decomposition, we acknowledge that the fine-scale details of the solution cannot be captured on a coarse grid. As it turns out, inaccuracies at the subgrid level may resonate and produce a numerical solution that is *globally* polluted with errors if one does not model subgrid effects correctly. We show that high-fidelity fine-scale solutions can be obtained by properly accounting for subgrid-scale heterogeneity.

Although the VMS formalism is general and can be applied to the continuum problem [5, 22, 26], here, we restrict our attention to the discrete fine-scale problem. Consider a *coarse* partition of the domain $\mathscr{T}_H = \bigcup_{i=1}^{N_H} E_i$ and the associated skeleton $\mathscr{S}_H = \bigcup_{a=1}^{M_H} \Gamma_a$ on which a coarse-scale discretization is defined, and the decomposition of the fine-scale solution:

$$\mathbf{u}_h = \mathbf{u}_H + \tilde{\mathbf{u}}, \tag{22}$$

$$p_h = p_H + \tilde{p}. \tag{23}$$

This decomposition is unique if we can express the original fine-scale solution space $V_h \times W_h$ as the direct sum of two spaces, with:

$$V_h = V_H \oplus \tilde{V}, \tag{24}$$

$$W_h = W_H \oplus \tilde{W}, \tag{25}$$

where $V_H \times W_H$ is the space of coarse scales and $\tilde{V} \times \tilde{W}$ is the space of subgrid scales. This decomposition allows one to split the fine-scale problem (18) and (19) into a coarse-scale problem and a subscale problem. Testing against coarse-scale test functions, we obtain the coarse-scale problem: Find $(\mathbf{u}_H, p_H) \in V_H \times W_H$ such that

$$(\mathbf{v}_H, \mathsf{k}^{-1}\mathbf{u}_H) + (\mathbf{v}_H, \mathsf{k}^{-1}\tilde{\mathbf{u}}) - (\nabla \cdot \mathbf{v}_H, p_H) - (\nabla \cdot \mathbf{v}_H, \tilde{p}) = -\langle \mathbf{v}_H \cdot \mathbf{n}, \bar{p} \rangle_{\Gamma_p}, \tag{26}$$

$$(w_H, \nabla \cdot \mathbf{u}_H) + (w_H, \nabla \cdot \tilde{\mathbf{u}}) = (w_H, f), \tag{27}$$

for all $\mathbf{v}_H \in V_H$ and $w_H \in W_H$. Testing against the subscale test functions and expressing the inner product as sums over coarse elements $E_i, i = 1, \ldots, N_H$, we arrive at the subscale problem: Find $(\tilde{\mathbf{u}}, \tilde{p}) \in \tilde{V} \times \tilde{W}$ such that

$$\sum_{i=1}^{N_H} \Big[(\tilde{\mathbf{v}}, \mathsf{k}^{-1}\mathbf{u}_H)_{E_i} + (\tilde{\mathbf{v}}, \mathsf{k}^{-1}\tilde{\mathbf{u}})_{E_i} - (\nabla \cdot \tilde{\mathbf{v}}, p_H)_{E_i} - (\nabla \cdot \tilde{\mathbf{v}}, \tilde{p})_{E_i} \Big] = -\sum_{i=1}^{N_H} \langle \tilde{\mathbf{v}} \cdot \mathbf{n}, \bar{p} \rangle_{\Gamma_p \cap \partial E_i}, \tag{28}$$

$$\sum_{i=1}^{N_H} \Big[(\tilde{w}, \nabla \cdot \mathbf{u}_H)_{E_i} \Big] + \sum_{i=1}^{N_H} \Big[(\tilde{w}, \nabla \cdot \tilde{\mathbf{u}})_{E_i} \Big] = \sum_{i=1}^{N_H} (\tilde{w}, f)_{E_i}. \tag{29}$$

for all $\tilde{\mathbf{v}} \in \tilde{V}$ and $\tilde{w} \in \tilde{W}$. We make the following remarks:

1. The solution obtained from the additive decompositions (22) and (23) above is exact; that is, the solution to Eqs. 26 and 27 and Eqs. 28 and 29 is the solution to the original fine-scale problems (18) and (19). This requires, however, the direct sum decompositions (24) and (25). In practice, the subscale spaces $\tilde{V}$ and $\tilde{W}$ are very difficult—if not impossible—to characterize.

2. The subgrid-scale problem (28)–(29) is an infinite dimensional, global problem. Therefore, in the form presented above, the complexity of the problem is the same as the original one.
3. The formulation is residual based in the sense that, if the coarse solution is the exact solution, the subscales vanish identically.
4. For the formulation to be advantageous from a computational viewpoint, we need a judicious choice of the coarse and subgrid approximation spaces, as well as a good localization assumption that will decouple the global subgrid problem into a set of local problems. These two key issues are addressed in the remainder of this section and in Section 4.

3.2 Choice of finite element spaces

Although this is by no means necessary, we assume for simplicity that the partitions $\mathcal{T}_h$ (fine grid) and $\mathcal{T}_H$ (coarse grid) are nested, conforming, and consist of rectangular elements. In other words, the coarse grid $\mathcal{T}_H$ results from a Cartesian upgridding of the fine grid $\mathcal{T}_h$. The target fine-scale approximation spaces are the lowest-order Raviart–Thomas space for the velocity, $V_h = RT_0(\mathcal{T}_h)$, and the space of piecewise constants for the pressure, $W_h = P_0(\mathcal{T}_h)$. We restrict our attention to coarse-scale velocity spaces that are compatible with a piecewise constant approximation of the pressure, $W_H = P_0(\mathcal{T}_H)$. The two obvious choices are $V_H = RT_0(\mathcal{T}_H)$ and the Brezzi–Douglas–Marini space of order 1, $V_H = BDM_1(\mathcal{T}_H)$ [14]. Both spaces satisfy the property $\operatorname{div} V_H = W_H$, and the inf-sup compatibility condition. In contrast with the choice made in [4], here, we use the low-order $RT_0(\mathcal{T}_H)$ space. Therefore, we define:

$$V_H = \left\{ \mathbf{v}_H : \mathbf{v}_H = \sum_{a=1}^{M_H} \mathbf{N}_a^H V_a, \quad V_b = 0 \, \forall \Gamma_b \in \Gamma_u \right\}, \tag{30}$$

$$W_H = \left\{ w_H : w_H = \sum_{i=1}^{N_H} \chi_i^H W_i \right\}, \tag{31}$$

where $\mathbf{N}_a^H$ is the RT_0 basis function associated with the coarse-element face Γ_a, V_a is the integrated coarse-scale flux through Γ_a, χ_i^H is the characteristic function for coarse element E_i, and W_i is the average pressure on coarse element E_i.

To mimic the fine-scale solution, the subgrid velocities are restricted to belong to the lowest-order Raviart–Thomas space on the fine grid within each coarse element. Let $E_{i,h} = \mathcal{T}_h(E_i)$ denote the fine grid defined over coarse element E_i. The subgrid-scale velocity field will be defined on each element satisfying the condition:

$$\tilde{V}_{E_i} \subset RT_0(E_{i,h}). \tag{32}$$

The elements of $\tilde{V}_{E_i}$ can be extended to all of Ω by zero, to define the subgrid velocity space as the direct sum of the subgrid spaces over coarse elements:

$$\tilde{V} = \bigoplus_{i=1}^{N_H} \tilde{V}_{E_i}. \tag{33}$$

Clearly, to have a continuous fine-scale velocity field, the subgrid velocity spaces must satisfy compatibility conditions on the skeleton of the coarse grid. This issue will be discussed in detail in the next subsection.

For consistency, the subgrid pressure space is restricted to belong to the space of discontinuous constant functions on each coarse element:

$$\tilde{W}_{E_i} \subset P_0(E_{i,h}). \tag{34}$$

An additional condition will be imposed to guarantee uniqueness of the solution. The elements of these spaces are extended by zero functions to the entire domain Ω, and the subgrid pressure space is then defined as:

$$\tilde{W} = \bigoplus_{i=1}^{N_H} \tilde{W}_{E_i}. \tag{35}$$

3.3 Localization of the subgrid problem

The essential requirement in the construction of our multiscale method is that *the approximation be locally conservative at both scales*; that is, it must satisfy the discrete version of the mass conservation statement on each element of the coarse and fine grids. This requirement leads to the condition:

$$(w_H, \nabla \cdot \mathbf{u}_H)_{E_i} = (w_H, f)_{E_i} \qquad \forall E_i \in \mathcal{T}_H, \tag{36}$$

or, equivalently, $\nabla \cdot \mathbf{u}_H = \Pi_H f$—the projection of the source term onto the space W_H of piecewise constants on the coarse grid. Substituting Eq. 36 in the coarse-scale equation (27) leads to

$$(w_H, \nabla \cdot \tilde{\mathbf{u}})_{E_i} = 0 \qquad \forall E_i \in \mathcal{T}_H. \tag{37}$$

As w_H is constant on each element, we can use the divergence theorem to translate Eq. 37 into the following *compatibility condition on the subgrid velocities*:

$$\boxed{\int_{\partial E_i} \tilde{\mathbf{u}} \cdot \mathbf{n} \, d\Gamma = 0 \qquad \forall E_i \in \mathcal{T}_H.} \tag{38}$$

Equation 38 is the essential condition that guarantees mass conservation at both scales and allows localizing the subgrid-scale problem. Of course, this condition can be immediately satisfied if one imposes $\tilde{\mathbf{u}} \cdot \mathbf{n} = 0$ on ∂E_i pointwise, as was done in [4] and [5], to define the subgrid velocity space on each element as follows:

$$\tilde{V}_{E_i,0} = \left\{\tilde{\mathbf{v}} : \tilde{\mathbf{v}} \in RT_0(E_{i,h}),\ \tilde{\mathbf{v}} \cdot \mathbf{n} = 0 \text{ on } \partial E_i\right\}. \tag{39}$$

However, this pointwise condition does not account for subgrid velocity variability across element interfaces. The important observation [26] is that such localization assumption is too stringent and, in fact, unnecessary: All that is required is that the subgrid velocities satisfy the weaker compatibility condition (38).

As a result, we approximate the global subgrid problems (28) and (29) as a set of Neumann problems on individual coarse elements. We make the following observations:

1. As we solve a Neumann problem on each coarse element E_i, the subgrid velocity test function $\tilde{\mathbf{v}}$ must satisfy $\tilde{\mathbf{v}} \cdot \mathbf{n} = 0$ on ∂E_i, which leads to the following orthogonality condition:

$$(\nabla \cdot \tilde{\mathbf{v}},\, p_H)_{E_i} = 0. \tag{40}$$

2. To guarantee uniqueness of the local subgrid problems, we define the space of subgrid pressure $\tilde{W}$ as the orthogonal complement of W_H in W_h:

$$\tilde{W} = W_H^{\perp} = \{\tilde{w} \in W_h : (\tilde{w}, w_H) = 0\ \forall w_H \in W_H\}. \tag{41}$$

As $W_H = \operatorname{div} V_H$, we have the additional orthogonality relation:

$$(\nabla \cdot \mathbf{v}_H,\, \tilde{p})_{E_i} = 0 \quad \text{or, equivalently} \quad \int_{E_i} \tilde{p}\, \mathrm{d}\Omega = 0. \tag{42}$$

In the light of the observations above, we define the following functional spaces on the fine grid $E_{i,h}$ of each coarse element:

$$\tilde{V}_{E_i,\tilde{u}} := \left\{\tilde{\mathbf{v}} \in RT_0(E_{i,h}),\ \tilde{\mathbf{v}} \cdot \mathbf{n} = \tilde{u} \text{ on } \partial E_i \text{ with } \int_{\partial E_i} \tilde{u}\, \mathrm{d}\Gamma = 0\right\}, \tag{43}$$

$$\tilde{W}_{E_i} := \left\{\tilde{w} \in P_0(E_{i,h}),\ \int_{E_i} \tilde{w}\, \mathrm{d}\Omega = 0\right\}. \tag{44}$$

The global subgrid spaces are defined through an extension to Ω by zero functions and a direct sum like in Eqs. 33 and 35.

3.4 Boundary conditions for the local subgrid problems

Using the compatibility condition (38) and the orthogonality conditions (40)–(42), the subgrid problem reads: For each coarse element $E_i = 1, \ldots, N_H$, find $(\tilde{\mathbf{u}}, \tilde{p}) \in \tilde{V}_{E_i,\tilde{u}} \times \tilde{W}_{E_i}$ such that

$$(\tilde{\mathbf{v}}, \mathsf{k}^{-1}\tilde{\mathbf{u}})_{E_i} - (\nabla \cdot \tilde{\mathbf{v}},\, \tilde{p})_{E_i} = -(\tilde{\mathbf{v}}, \mathsf{k}^{-1}\mathbf{u}_H)_{E_i}, \tag{45}$$

$$(\tilde{w}, \nabla \cdot \tilde{\mathbf{u}})_{E_i} = (\tilde{w},\, f - \nabla \cdot \mathbf{u}_H)_{E_i}. \tag{46}$$

for all $\tilde{\mathbf{v}} \in \tilde{V}_{E_i,0}$ and $\tilde{w} \in \tilde{W}_{E_i}$. Given $\mathbf{u}_H$ and the local boundary conditions $\tilde{u}_{E_i}$ (to be discussed next), the problem above has a unique solution. The global subgrid scale solution $(\tilde{\mathbf{u}}, \tilde{p})$ is then obtained by patching together the solutions on each coarse element.

In the remaining of this section, we shall restrict our attention to the case when the source function does not display a multiscale character. Mathematically, this means that the source function is equal to its projection on the space of coarse-scale pressures:

$$(w_H,\, f) = (w_H,\, 1)\, f \quad \text{for all } w_H \in W_H, \tag{47}$$

or, equivalently,

$$f = \Pi_H f = f_H = \nabla \cdot \mathbf{u}_H. \tag{48}$$

Under these conditions, the right-hand side of Eq. 46 is equal to zero. Clearly, the case in which Eq. 48 is not satisfied is important in the presence of wells, and it is discussed at length in Section 4.

3.4.1 No subgrid communication

Consider first the choice of zero subgrid flux across coarse elements, $\tilde{u} = 0$ on ∂E for all $E \in \mathscr{T}_H$ [4, 5]. Recalling Eq. 30, the subgrid solution inside element E takes the form:

$$\tilde{\mathbf{u}} = \sum_a \tilde{\mathbf{N}}_a^0 U_a, \tag{49}$$

$$\tilde{p} = \sum_a \tilde{\phi}_a^0 U_a. \tag{50}$$

where $\left(\tilde{\mathbf{N}}_a^0, \tilde{\phi}_a^0\right) \in \tilde{V}_{E,0} \times \tilde{W}_E$ is the solution to:

$$\left(\tilde{\mathbf{v}}, \mathsf{k}^{-1}\tilde{\mathbf{N}}_a^0\right)_E - \left(\nabla \cdot \tilde{\mathbf{v}}, \tilde{\phi}_a^0\right)_E = -\left(\tilde{\mathbf{v}}, \mathsf{k}^{-1}\mathbf{N}_a^H\right)_E \quad \forall \tilde{\mathbf{v}} \in \tilde{V}_{E,0}, \tag{51}$$

$$\left(\tilde{w}, \nabla \cdot \tilde{\mathbf{N}}_a^0\right)_E = 0 \quad \forall \tilde{w} \in \tilde{W}_E. \tag{52}$$

This solution is referred to as a subgrid numerical Green function [4]. Equations 49 and 50 show that the subgrid solution scales linearly with the coarse-scale fluxes U_a.

3.4.2 Proposed subgrid communication

If subgrid communication between coarse elements is disallowed, the subgrid velocity is restricted to recirculation functions within each coarse element. This localization assumption clearly limits the ability of the method to capture thin but long-range permeability structures that span more than one coarse element. In general, if $\tilde{u} \neq 0$ on ∂E, the subgrid solution takes the form:

$$\tilde{\mathbf{u}} = \tilde{\mathbf{u}}_{\text{skel}} + \sum_a \tilde{\mathbf{N}}_a^0 U_a, \tag{53}$$

$$\tilde{p} = \tilde{p}_{\text{skel}} + \sum_a \tilde{\phi}_a^0 U_a, \tag{54}$$

where $(\tilde{\mathbf{u}}_{\text{skel}}, \tilde{p}_{\text{skel}})$ reflects the influence of the local subgrid boundary conditions. We design these to satisfy the following conditions:

1. Lead to a flux-continuous (conforming) velocity field.
2. Result in a discretization that is locally mass-conservative at both scales.
3. Reflect the fine-scale heterogeneity.
4. Be computable without knowledge of the global velocity field.

Condition 1 will be satisfied if the subgrid flux is uniquely defined on the skeleton $\mathscr{S}_H$ of the coarse grid $\mathscr{T}_H$. An easy way to ensure condition 2 is to impose that the subscale flux satisfy:

$$\int_{\Gamma_a} \tilde{u} \, \mathrm{d}\Gamma = 0 \qquad \forall \Gamma_a \in \mathscr{S}_H. \tag{55}$$

Condition 3 requires that the subscale velocity be a solution to local problems using the fine-scale permeability k. In an attempt to satisfy condition 4, we let the subgrid flux on each coarse edge scale with the coarse flux through that edge. Equations 53 and 54 are then rewritten as:

$$\tilde{\mathbf{u}} = \sum_a \left(\tilde{\mathbf{N}}_a^{\text{skel}} + \tilde{\mathbf{N}}_a^0\right) U_a = \sum_a \tilde{\mathbf{N}}_a U_a, \tag{56}$$

$$\tilde{p} = \sum_a \left(\tilde{\phi}_a^{\text{skel}} + \tilde{\phi}_a^0\right) U_a = \sum_a \tilde{\phi}_a U_a. \tag{57}$$

Therefore, we can define the multiscale velocity as the sum of the coarse-scale and subgrid-scale components:

$$\mathbf{u}_{H,h} = \mathbf{u}_H + \tilde{\mathbf{u}} = \sum_a \left(\mathbf{N}_a^H + \tilde{\mathbf{N}}_a\right) U_a = \sum_a \mathbf{N}_a^{H,h} U_a, \tag{58}$$

where $\mathbf{N}_a^{H,h}$ is the multiscale velocity basis function associated with interface Γ_a. Different definitions of the multiscale basis functions exist [1, 2, 16], and in this work, we have adopted the recent one proposed by [27], where the multiscale basis function is the solution to a flow problem restricted to a pair of adjacent coarse elements with source terms specified in such a way that the flow through the interface is identically one (see Fig. 1). More precisely, the multiscale basis functions $(\mathbf{N}_a^{H,h}, \phi_a^{H,h})$ for interface Γ_a (common to coarse elements E_i and E_j) are the solution to the following local problem:

$$\mathsf{k}^{-1}\mathbf{N}_a^{H,h} + \nabla\phi_a^{H,h} = 0 \qquad \text{in } E_i \cup E_j, \tag{59}$$

$$\nabla \cdot \mathbf{N}_a^{H,h} = \begin{cases} w(x) \Big/ \displaystyle\int_{E_i} w(x) \, \mathrm{d}\Omega & \text{if } x \in E_i, \\ -w(x) \Big/ \displaystyle\int_{E_j} w(x) \, \mathrm{d}\Omega & \text{if } x \in E_j, \end{cases} \tag{60}$$

$$\mathbf{N}_a^{H,h} \cdot \mathbf{n} = 0 \qquad \text{on } \partial(E_i \cup E_j). \tag{61}$$

In [27], it is suggested that the source function $w(x)$ be scaled with the trace of the permeability tensor, $\operatorname{trace}\mathsf{k}(x)$. To ensure that the method is mass conservative at the coarse and subscale level, we impose the following scaling for $w(x)$ on each element:

$$w(x) = \begin{cases} \operatorname{trace}\mathsf{k}(x) & \text{if } \Pi_H f = 0, \\ 1 & \text{if } \Pi_H f \neq 0. \end{cases} \tag{62}$$

It is important to observe that the coarse-scale RT_0 basis functions are in fact solutions to Eqs. 59–62 with $\mathsf{k}(x) = \text{constant}$ and $w(x) = 1$.

Proposition *If we define the subscale basis functions on each element E_i as:*

$$\tilde{\mathbf{N}}_a = \mathbf{N}_a^{H,h} - \mathbf{N}_a^H, \tag{63}$$

$$\tilde{\phi}_a^{E_i} = \phi_a^{H,h} - \frac{1}{|E_i|} \int_{E_i} \phi_a^{H,h} \, \mathrm{d}\Omega, \tag{64}$$

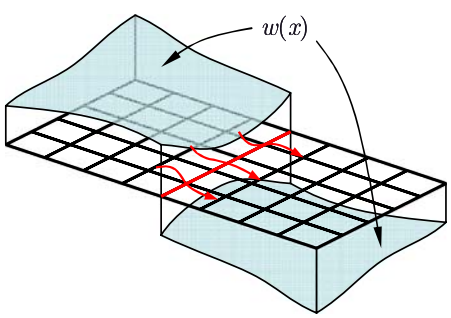

Fig. 1 Diagram illustrating the local flow problem defining the multiscale basis functions

then

$$\tilde{\mathbf{u}} = \sum_a \tilde{\mathbf{N}}_a U_a, \tag{65}$$

$$\tilde{p} = \sum_a \tilde{\phi}_a^{E_i} U_a, \tag{66}$$

is a solution to the subgrid problem (45)–(46).

Proof We first show that solutions (65)–(66) satisfy the mass balance equation (46). Recall that we consider the case with a source function $f = \Pi_H f$ only. The case $f \notin W_H$ will be treated in Section 4. Under this assumption, Eq. 46 reduces to

$$(\tilde{w}, \nabla \cdot \tilde{\mathbf{u}})_E = 0 \quad \forall \tilde{w} \in \tilde{W}_E \tag{67}$$

or, equivalently,

$$\sum_a U_a (\tilde{w}, \nabla \cdot \tilde{\mathbf{N}}_a)_E = 0 \quad \forall \tilde{w} \in \tilde{W}_E. \tag{68}$$

We must consider two cases:

1. Zero source on element E, $\Pi_H f = 0$. In this case, mass conservation on the coarse scale implies

$$\nabla \cdot \mathbf{u}_H = 0 \text{ on } E \Rightarrow \int_{\partial E} \mathbf{u}_H \cdot \mathbf{n} \, \mathrm{d}\Gamma = 0$$
$$\Rightarrow \sum_a U_a = 0. \tag{69}$$

   Under this condition, Eq. 68 is satisfied as long as $\nabla \cdot \tilde{\mathbf{N}}_a$ is a function of position, but independent of the face a. This is indeed satisfied by our definition of the multiscale basis functions with $w(x)$ given by Eq. 62.
2. Nonzero source on element E, $\Pi_H f \neq 0$. In this case, Eq. 69 does not hold, and Eq. 68 implies

$$(\tilde{w}, \nabla \cdot \tilde{\mathbf{N}}_a)_E = 0 \quad \forall \tilde{w} \in \tilde{W}_E. \tag{70}$$

   for all $\Gamma_a \in \partial E$ individually. This condition, together with Equation 55, implies that $\nabla \cdot \tilde{\mathbf{N}}_a \equiv 0$ on E. Once again, this is satisfied by our definition of the source function in Eq. 62.

We now need to show that $(\tilde{\mathbf{u}}, \tilde{p})$ defined in Eqs. 65 and 66 satisfy the Darcy equation (45). First we note that, by virtue of Eqs. 63 and 64,

$$\int_{\Gamma_a} \tilde{\mathbf{N}}_a \cdot \mathbf{n} \, \mathrm{d}\Gamma = 0, \quad \int_E \tilde{\phi}_a^E \, \mathrm{d}\Omega = 0. \tag{71}$$

Therefore, $(\tilde{\mathbf{u}}, \tilde{p}) \in \tilde{V}_{E,\tilde{u}} \times \tilde{W}_E$ independently of the coarse-scale fluxes U_a. Using integration by parts, we write Eq. 45 in strong form:

$$\mathsf{k}^{-1}\tilde{\mathbf{u}} + \nabla \tilde{p} = -\mathsf{k}^{-1}\mathbf{u}_H \text{ in } E \tag{72}$$

or, equivalently:

$$\sum_a U_a \left(\mathsf{k}^{-1} \mathbf{N}_a^{H,h} + \nabla \phi_a^{H,h} \right) = 0 \text{ in } E. \tag{73}$$

Indeed, the term in parenthesis is identically equal to zero by Eq. 59. This completes the proof. □

Remark The local problems (59–61) can be solved using a low-order (RT_0) mixed finite element method or a finite volume method. Clearly, for constant k, the multiscale basis function reduces to the common RT_0 basis function, and the subgrid basis function is identically equal to zero. In the presence of subgrid heterogeneity, the subgrid basis function will capture not only flow redistribution within the coarse element, but also preferential flow across the interface.

A slightly modified problem needs to be solved for the multiscale basis function at a face Γ_a on the boundary of the domain. If $\Gamma_a \subset \Gamma_p$, we solve the same local problem (59)–(61), with an imaginary coarse element whose permeability is a reflection (with respect to Γ_a) of the permeability of the element inside the domain. Although our description in this paper is restricted to the case of zero prescribed flux, $\bar{u} = 0$, our implementation certainly allows for $\bar{u} \neq 0$. In that case, if $\Gamma_a \subset \Gamma_u$, we solve the following local problem:

$$\mathsf{k}^{-1}\mathbf{N}_a^{H,h} + \nabla \phi_a^{H,h} = 0 \qquad \text{in } E_i, \tag{74}$$

$$\nabla \cdot \mathbf{N}_a^{H,h} = -w(x) \Big/ \int_{E_i} w(x) \, \mathrm{d}\Omega, \tag{75}$$

$$\mathbf{N}_a^{H,h} \cdot \mathbf{n} = \begin{cases} 0 & \text{on } \partial E_i \setminus \Gamma_a, \\ \bar{u} \Big/ \int_{\Gamma_a} \bar{u} \, \mathrm{d}\Gamma & \text{on } \Gamma_a, \end{cases} \tag{76}$$

We note that the multiscale basis function may differ from the RT_0 coarse basis function due to subgrid variability of either the permeability k or the prescribed flux $\bar{u}$. Our definition ensures that the fine-scale boundary fluxes are honored exactly.

3.5 The coarse-scale problem revisited

Making use of the compatibility condition (37) and the orthogonality relation (42), the coarse-scale problems

(26) and (27) read: Find $(\mathbf{u}_H, p_H) \in V_H \times W_H$ such that

$$(\mathbf{v}_H, \mathsf{k}^{-1}\mathbf{u}_H) + (\mathbf{v}_H, \mathsf{k}^{-1}\tilde{\mathbf{u}}) - (\nabla \cdot \mathbf{v}_H, p_H) = -\langle \mathbf{v}_H \cdot \mathbf{n}, \bar{p}\rangle_{\Gamma_p}, \tag{77}$$

$$(w_H, \nabla \cdot \mathbf{u}_H) = (w_H, f), \tag{78}$$

for all $\mathbf{v}_H \in V_H$ and $w_H \in W_H$. It is interesting to note that the subgrid contribution to the coarse-scale problem, albeit essential, is confined to the second term of Eq. 77.

This form of the problem is nonsymmetric. In practice, it is convenient to express it as an *equivalent*, symmetric problem. For this purpose, we define the multiscale velocity and pressure space functions:

$$V_{H,h} = \left\{ \mathbf{v}_{H,h} : \mathbf{v}_{H,h} = \sum_{a=1}^{M_H} \mathbf{N}_a^{H,h} V_a, \quad V_b = 0 \; \forall \Gamma_b \in \Gamma_u \right\}, \tag{79}$$

$$W_{H,h} = W_H \oplus \tilde{W} = \left\{ w_{H,h} : w_{H,h} = \sum_{i=1}^{N_H} \chi_i^H \left(W_i + \sum_a \tilde{\phi}_a^{E_i} V_a \right) \right\}, \tag{80}$$

Proposition *The coarse scale problem* (77)–(78) *can be written in the following equivalent, symmetric form: Find* $(\mathbf{u}_{H,h}, p_{H,h}) \in V_{H,h} \times W_{H,h}$ *such that*

$$(\mathbf{v}_{H,h}, k^{-1}\mathbf{u}_{H,h}) - (\nabla \cdot \mathbf{v}_{H,h}, p_{H,h}) = -\langle \mathbf{v}_{H,h} \cdot \mathbf{n}, \bar{p}\rangle_{\Gamma_p}, \tag{81}$$

$$(w_{H,h}, \nabla \cdot \mathbf{u}_{H,h}) = (w_{H,h}, f), \tag{82}$$

for all $\mathbf{v}_{H,h} \in V_{H,h}$ *and* $w_{H,h} \in W_{H,h}$.

Proof We first show that Eqs. 77 and 81 are equivalent. The first term in Eq. 81 can be written as:

$$(\mathbf{v}_{H,h}, \mathsf{k}^{-1}\mathbf{u}_{H,h}) = (\mathbf{v}_H, \mathsf{k}^{-1}\mathbf{u}_{H,h}) + (\tilde{\mathbf{v}}, \mathsf{k}^{-1}\mathbf{u}_{H,h}). \tag{83}$$

Exploiting the orthogonality properties $\operatorname{div} V_H \perp \tilde{W}$ and $\operatorname{div} \tilde{V} \perp W_H$ and integration by parts, the second term reads:

$$-(\nabla \cdot \mathbf{v}_{H,h}, p_{H,h}) = -(\nabla \cdot \mathbf{v}_H, p_H) + (\tilde{\mathbf{v}}, \nabla \tilde{p}) - \langle \tilde{\mathbf{v}} \cdot \mathbf{n}, \bar{p}\rangle_{\Gamma_p}. \tag{84}$$

Inserting the two equations above in Eq. 81, we obtain:

$$(\mathbf{v}_H, \mathsf{k}^{-1}\mathbf{u}_{H,h}) - (\nabla \cdot \mathbf{v}_H, p_H) + (\tilde{\mathbf{v}}, \mathsf{k}^{-1}\mathbf{u}_{H,h} + \nabla \tilde{p}) = -\langle \mathbf{v}_H \cdot \mathbf{n}, \bar{p}\rangle_{\Gamma_p}. \tag{85}$$

The third term in the equation above vanishes due to our definition of the subgrid problem, so we have arrived at Eq. 77.

We now show the equivalence of Eqs. 77 and 82. Exploiting the orthogonality properties once again and recalling that, in this section, we are considering the case $f = \Pi_H f$ only, Eq. 82 takes the form:

$$(w_H, \nabla \cdot \mathbf{u}_H) + (\tilde{w}, \nabla \cdot \tilde{\mathbf{u}}) = (w_H, f). \tag{86}$$

The second term vanishes due to the imposed mass conservation at the fine scale (see Eq. 67 and the subsequent discussion). This completes the proof. □

3.6 A multiscale method with a coarse pressure approximation

The proposition above shows that, for the case in which the source term does not display fine-scale variability, our variational multiscale mixed finite element (VMSMFE) method is equivalent to a multiscale mixed finite element method. This observation was made in [6] for the case when subgrid communication was disallowed (they also treated a method with oversampling that leads to a nonconforming fine-scale velocity field). Numerical results from the solution of Eqs. 77 and 78 (or their symmetric equivalent [Eqs. 81 and 82]) were given in [26]. Further experimentation has shown that improved results are obtained when the pressure space is restricted to belong to the space of piecewise constant functions on the *coarse* grid.

The problem to be solved is essentially identical to Eqs. 81 and 82, except that the solution space for the pressure is W_H instead of $W_{H,h}$: Find $(\mathbf{u}_{H,h}, p_H) \in V_{H,h} \times W_H$ such that

$$(\mathbf{v}_{H,h}, \mathsf{k}^{-1}\mathbf{u}_{H,h}) - (\nabla \cdot \mathbf{v}_{H,h}, p_H) = -\langle \mathbf{v}_{H,h} \cdot \mathbf{n}, \bar{p}\rangle_{\Gamma_p}, \tag{87}$$

$$(w_H, \nabla \cdot \mathbf{u}_{H,h}) = (w_H, f), \tag{88}$$

for all $\mathbf{v}_{H,h} \in V_{H,h}$ and $w_H \in W_H$.

In the absence of a source term with multiscale character, this method is precisely the multiscale mixed finite element method proposed in [27]. Our method differs in its derivation (the VMS framework rather than the multiscale finite element method) and, more importantly, in the treatment of fine-scale sources. The improved behavior is not only restricted to the pressure solution, but also to the velocity field, as both fields are coupled. In any case, the fine-scale pressure can still be reconstructed according to the multiscale decomposition (23) with $\tilde{p}$ given by Eq. 66 once the solution has been computed. This step does not carry any additional computational cost, as the subgrid-scale pressure basis

functions are obtained together with the velocity basis functions.

3.6.1 Implementation

The implementation of the VMSMFE method is relatively straightforward. It consists of the following steps:

1. Precompute the multiscale basis functions ($\mathbf{N}_a^{H,h}$, $\phi_a^{H,h}$) for each coarse interface Γ_a.
2. Build the system of equations corresponding to the coarse-scale problems (87) and (88):

$$\begin{bmatrix} \mathsf{A} & -\mathsf{B}^t \\ \mathsf{B} & 0 \end{bmatrix} \begin{bmatrix} \mathsf{U} \\ \mathsf{P} \end{bmatrix} = \begin{bmatrix} \mathsf{g} \\ \mathsf{f} \end{bmatrix}, \tag{89}$$

   to be solved for the coarse-scale interface fluxes $\mathsf{U} = \{U_a\}$ and cell-center pressures $\mathsf{P} = \{P_i\}$. The system incorporates the subgrid-scale contributions in matrix A, obtained by assembly of the coarse-element contributions:

$$A_{ab}^E = \int_E \mathbf{N}_a^{H,h} \mathsf{k}^{-1} \mathbf{N}_b^{H,h} \, \mathrm{d}\Omega. \tag{90}$$

   As both the permeability tensor and the basis functions display a multiscale character, the integrals must be evaluated on the underlying fine grid. The matrix is symmetric, as it corresponds to the symmetric form of the problem.
3. Reconstruct the fine-scale velocity and pressure fields resorting to the additive decompositions (22) and (23). The subgrid part is obtained by linear combination of the (known) coarse-scale fluxes and (precomputed) subgrid-scale basis functions.

4 Multiscale source terms

In this section, we shall examine the case when the source/sink term presents a multiscale character. This is a scenario of paramount importance because, in practice, flow is driven by injection and production wells. Wells are features that are much smaller than the resolution that one can afford in field-scale simulations and should, therefore, be understood as concentrated (point or line) sources. A well model relates the flow rate into or out of the well with the difference between the wellbore pressure and the average pressure of the well gridblock. An analytical representation of such relationship is possible in simplified cases—in particular, when the well block is assumed to be homogeneous [8, 30]. In a multiscale method that attempts to capture subgrid variability, two things are needed:

1. A computational strategy to handle *concentrated sources* with variability at the scale of the fine grid.
2. A *well model* that relates flow rate with the pressure difference between the wellbore and the fine well block.

In this paper, we concentrate exclusively on the first issue and assume that the source term is a function that displays variability at the scale of the fine grid. In particular, we shall assume that the source term f belongs to the space of piecewise constant functions on the fine grid:

$$f = \Pi_h f \in W_h. \tag{91}$$

To fully account for the presence of wells, standard well models can then be used at the fine scale.

As this is a case of practical interest, we shall understand that f consists of a number of concentrated sources:[1]

$$f(x) = \sum_{j=1}^{N_w} f_j(x). \tag{92}$$

Each f_j is a concentrated source/sink that is constant on a fine scale gridblock e_j, inside a coarse block E_j. Of course, several wells may exist within the same coarse block. In Section 3, we presented a VMS method for the solution of the problem without fine wells; that is, when the sources where assumed to be spread over coarse elements, $f = \Pi_H f = 0$. In this section, we extend the formulation to consider subgrid variations of the source term,

$$\tilde{f} := f - \Pi_H f \neq 0, \tag{93}$$

while preserving mass conservation at both coarse and subgrid scales.

4.1 Principle

We start by decomposing the source term into its coarse scale and subscale components:

$$f = f_H + \tilde{f}, \tag{94}$$

where $f_H \in W_H$ and $\tilde{f} \in \tilde{W}$. The subscale component is simply the deviatoric (zero-mean) part of f on each

[1] In what follows, we shall abuse language and refer to 'wells' when, strictly speaking, we mean 'concentrated or point sources'.

coarse element. It is then natural to decompose the full multiscale solution as follows:

$$\mathbf{u}_{H,h}^{\text{well}} = \mathbf{u}_{H,h} + \mathbf{u}^{\text{well}}, \tag{95}$$

$$p_{H,h}^{\text{well}} = p_{H,h} + p^{\text{well}}, \tag{96}$$

where $(\mathbf{u}_{H,h}, p_{H,h})$ is the solution to a problem with coarse source terms f_H and $(\mathbf{u}^{\text{well}}, p^{\text{well}})$ is the solution to a problem with deviatoric fine-scale sources $\tilde{f}$. Special care must be taken of the prescribed-pressure boundary conditions. As we will see, the well problem is defined as a Neumann problem with deviatoric sources on each element and zero-flux boundary conditions. This results in certain pressures at the boundary, $\bar{p}^{\text{well}}$. The multiscale solution must then be seen as the solution to the original problem, but with coarse sources and with pressure boundary conditions replaced by $\bar{p} - \bar{p}^{\text{well}}$.

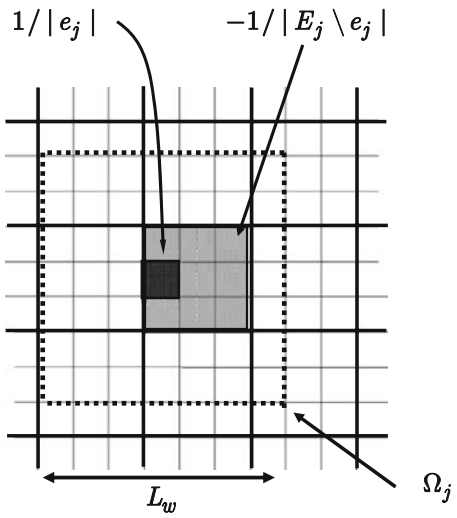

Fig. 2 Diagram illustrating the local flow problem defining the well basis functions

4.2 The local well problem

Recall the decomposition of the source term into individual wells $j = 1, \ldots, N_w$. We express the well solution as

$$\mathbf{u}^{\text{well}} = \sum_{j=1}^{N_w} Q_j \boldsymbol{\psi}_j^{\text{well}}, \tag{97}$$

$$p^{\text{well}} = \sum_{j=1}^{N_w} Q_j \varphi_j^{\text{well}}, \tag{98}$$

where Q_j is the strength of each well:

$$Q_j = \int_{e_j} f(x)\, \mathrm{d}x = f_j |e_j|, \tag{99}$$

and $\boldsymbol{\psi}_j^{\text{well}}$ and φ_j^{well} are the well velocity and pressure basis functions, respectively.

To maintain the computational complexity of the multiscale method, we assume that the well functions have local support in a subdomain Ω_j that is equal to or larger than coarse block E_j containing the well; that is, $e_j \subset E_j \subseteq \Omega_j$. More precisely, the well basis functions $(\boldsymbol{\psi}_j^{\text{well}}, \varphi_j^{\text{well}})$ for well j are the solution to the following problem:

$$\mathsf{k}^{-1} \boldsymbol{\psi}_j^{\text{well}} + \nabla \varphi_j^{\text{well}} = 0 \qquad \text{in } \Omega_j, \tag{100}$$

$$\nabla \cdot \boldsymbol{\psi}_j^{\text{well}} = \begin{cases} \dfrac{1}{|e_j|} - \dfrac{1}{|E_j|} & \text{if } x \in e_j \\ -\dfrac{1}{|E_j|} & \text{if } x \in E_j \setminus e_j \\ 0 & \text{if } x \in \Omega_j \setminus E_j \end{cases} \tag{101}$$

$$\boldsymbol{\psi}_j^{\text{well}} \cdot \mathbf{n} = 0 \qquad \text{on } \partial\Omega_j. \tag{102}$$

From an implementation standpoint, the well region Ω_j is a group of elements surrounding the fine well block e_j (see Fig. 2). The actual size of Ω_j is determined by setting a length scale parameter L_w. We choose to express this length scale as a fraction N_l of the characteristic dimension of the domain, L_Ω, such that:

$$L_w = N_l L_\Omega. \tag{103}$$

Clearly, a larger L_w will allow for a more accurate representation of the well effects, at the cost of increasing the computational cost. In the numerical simulations of the next section, we typically choose values between $N_l = 1/16$ and $N_l = 1/4$. Near boundaries, the well region is always restricted to lie inside the domain.

4.3 The coarse-scale problem revisited

The solution of the fine-scale well problem as proposed here is independent of the multiscale problem with coarse source terms. Once the well basis functions $(\boldsymbol{\psi}_j^{\text{well}}, \varphi_j^{\text{well}})$ have been computed for all wells and the fine-scale well solution constructed by linear combination through Eqs. 97 and 98, the pressure at the boundary $\bar{p}^{\text{well}}$ is recorded.

The coarse-scale problems (87) and (88) must be modified only to replace the source function by its gridblock-averaged counterpart and to incorporate the (subgrid-scale) influence of wells on boundaries with prescribed pressure.

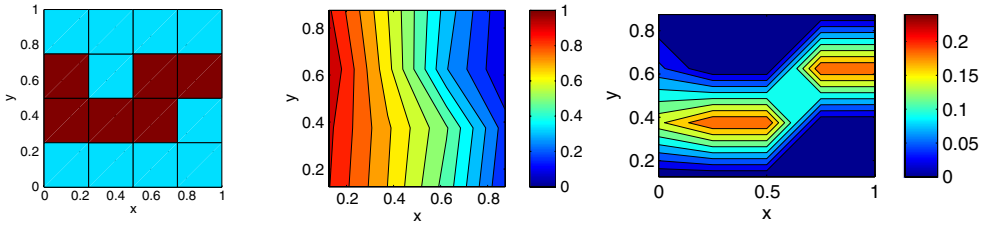

a permeability **b** pressure **c** flux in x-direction

Fig. 3 Small channelized system. Fine-scale finite volume solution

The coarse-scale problem reads: Find $(\mathbf{u}_{H,h}, p_H) \in V_{H,h} \times W_H$ such that

$$(\mathbf{v}_{H,h}, \mathsf{k}^{-1}\mathbf{u}_{H,h}) - (\nabla \cdot \mathbf{v}_{H,h}, p_H) = -\langle \mathbf{v}_{H,h} \cdot \mathbf{n}, \bar{p} - \bar{p}^{\text{well}} \rangle_{\Gamma_p}, \tag{104}$$

$$(w_H, \nabla \cdot \mathbf{u}_{H,h}) = (w_H, f_H), \tag{105}$$

for all $\mathbf{v}_{H,h} \in V_{H,h}$ and $w_H \in W_H$. Once the coarse-scale problem has been computed, the full solution is given by Eqs. 95 and 96.

This formulation—based on introducing additional basis functions associated with each well—removes the singularities from the multiscale problem due to the presence of wells. Our definition of the (local) well problems as Neumann problems with a deviatoric source in the coarse well block leads to a mass conservative velocity at both scales. An important feature of our formulation is that well regions are allowed to overlap without compromising mass conservation or flux continuity, which gives flexibility with regard to the choice of the well length scale.

5 Numerical simulations

In this section, we illustrate the performance of the VMSMFE method in several cases of increasing complexity. We restrict our attention to examples in two dimensions with uniform rectangular grids. To assess the accuracy and robustness of the method with respect to heterogeneity, meshes and wells, we compare the solutions obtained using the proposed multiscale method with the reference fine-scale solution obtained using a two-point finite volume method.

We compute a mean pressure error in the following manner:

$$\varepsilon(p) = \frac{\|\mathsf{p} - \mathsf{p}^{\text{ref}}\|^2}{\|\mathsf{p}^{\text{ref}}\|^2}, \tag{106}$$

where p and p^{ref} are array vectors that contain the average pressure in each fine element (multiscale solution and reference finite volume solution, respectively) and $\|\cdot\|$ is the usual discrete l^2 norm. The velocity error is computed as:

$$\varepsilon(\mathbf{u}) = \frac{\|\mathsf{u}_x - \mathsf{u}_x^{\text{ref}}\|^2}{\|\mathsf{u}_x^{\text{ref}}\|^2} + \frac{\|\mathsf{u}_y - \mathsf{u}_y^{\text{ref}}\|^2}{\|\mathsf{u}_y^{\text{ref}}\|^2}, \tag{107}$$

where u_x and u_y are array vectors that contain the average velocities across the fine mesh interfaces in the x- and y-directions.

5.1 Small channelized system

The first example illustrates the ability of the method to capture the global and detailed flow pattern in the presence of drastic subgrid heterogeneity. The fine grid is just a 4×4 grid, with isotropic permeability field shown in Fig. 3a. The red blocks are highly conductive ($k = 1$), and the blue blocks correspond to low permeability ($k = 10^{-3}$). Flow is left to right, with the left boundary set at a pressure $\bar{p}_{\text{left}} = 1$ and the right

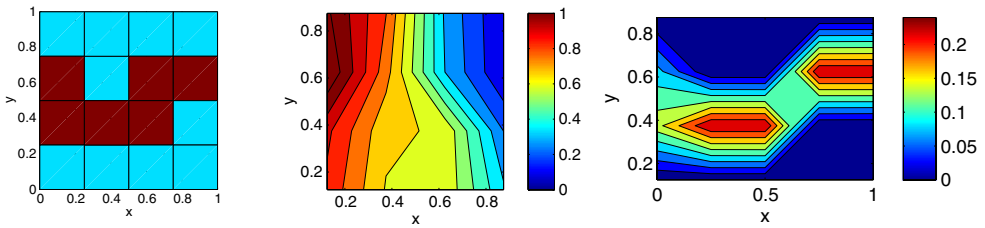

a permeability **b** pressure **c** flux in x-direction

Fig. 4 Small channelized system. VMS solution on a 2×2 coarse grid

boundary at $\bar{p}_{\text{right}} = 0$. The top and bottom boundaries are no-flow boundaries.

The pressure and flux in the x-direction from a finite volume solution computed on the fine grid are shown in Fig. 3. The contours of x-flux clearly indicate the preferential flow path along the high-conductivity channel. In Fig. 4, we show the solution obtained using the VMSMFE method on a coarse grid of 2×2 elements. The multiscale solution captures the sharp contrast in permeability, although there is no scale separation at all (the high-permeability channel spans the entire domain).

The fine-scale finite volume solution predicts an overall flow rate across the domain of 0.2064 and the VMS solution a flow rate of 0.2422 (a 17% error). For comparison, the flow rate computed with the finite volume method on a refined grid of 16×16 elements is 0.2477. This represents a 17% difference with respect to the flow rate computed on a 4×4 grid on which the permeability is defined. In this particular case, the error between VMS and fine-scale finite volume solutions is thus of the same order as the error between finite volume solutions on the fine-scale and on the refined grid. In the examples that follow, the VMS solution on a number of coarse grids is compared only with the finite volume solution on the original fine grid in which the permeability is defined.

5.2 Quarter five-spot simulations

In this study, we show results for corner-to-corner flow in a two-dimensional unit square geometry, a configuration known as a quarter of a five-spot pattern. Injector and producer are located in diagonally opposite vertices of the grid (Fig. 5), and all boundaries are no-flow boundaries. Wells at the corners of the domain are modeled as source/sink terms over the fine-scale corner grid block. We used a fine grid of 64×64 elements.

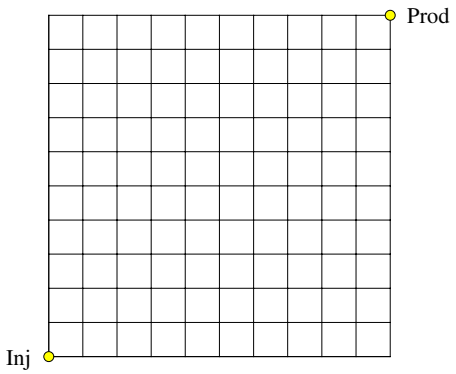

Fig. 5 Schematic of the quarter five-spot problem

The objective of this section is to study the performance of the proposed VMS formulation for:

- Different heterogeneous permeability fields: smoothly varying and channelized.
- A variety of coarse meshes: from 2- to 16-fold upgridding in each direction ($N = 32 \times 32$ to 4×4, respectively).
- Various choices of the well length scale: well region ranging from 2×2 to 16×16 fine blocks ($N_l = 1/32$ to $1/4$, respectively).

5.2.1 Isotropic correlation structure

In this heterogeneous structure, the permeability is isotropic and log-normally distributed with dimensionless correlation length equal to 0.1 in each direction, and $\sigma^2_{\log \mathsf{k}} \approx 1.0$. The permeability field is shown in Fig. 6.

In Fig. 7, we plot the velocity and pressure errors for different coarse discretizations and well length scales used to compute the fine well contributions. As expected, the error decreases with increasing number of coarse cells. In this case, the multiscale solutions are fairly independent of the well length scale, although larger support for the well basis function results in slightly smaller error.

5.2.2 System with vertical channels

In this study, we present results for a highly heterogeneous system (the permeability varies over 8 orders of magnitude) in which the heterogeneity is dominated by a large correlation length (about 1.0) in the y-direction. The correlation length in the x-direction is around 0.1, as before. The log-permeability map is shown in Fig. 8.

The velocity and pressure errors are shown in Fig. 9. The pressure error decreases monotonically, as the coarse grid is refined, and it decreases also (albeit slightly) with increasing well length scale. The velocity error displays a somewhat different behavior: The error is larger for a coarse grid of 8×8 or 16×16 elements than for a coarse grid of 4×4 elements. The reason is that, due to the drastic changes in permeability in the x-direction, the VMSMFE exhibits a mild resonance effect for coarse discretizations of the same length scale as the x-correlation length.

5.2.3 System with diagonal channels

Similar observations apply for a heterogeneous permeability field with large correlation length in the diagonal direction (Fig. 10). The pressure error decreases

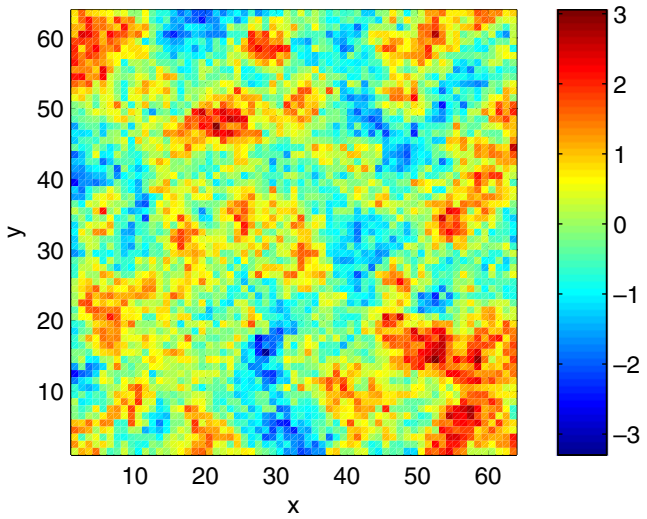

Fig. 6 Log-permeability field for the isotropic correlation structure

monotonically with increasing refinement of the coarse grid and well length scale. The velocity error, on the other hand, is small but does not exhibit a clear trend with respect to the coarse discretization (Fig. 11).

5.3 Study of anisotropy

It has been reported recently [27, 29] that some multiscale methods have difficulty in producing high quality solutions in the presence of permeability anisotropy or large aspect ratios of the grid (both cases are common in reservoir models). In this study, we demonstrate the ability of our proposed method to cope with these scenarios. We consider diagonal permeability tensors

$$\mathsf{k} = \begin{pmatrix} k_{xx} & 0 \\ 0 & k_{yy} \end{pmatrix}, \tag{108}$$

where $\alpha = k_{yy}/k_{xx}$ is the anisotropy ratio. To fully explore the effect of anisotropy, we used values of α ranging from 0.01 to 100 (the same value of α is used for all gridblocks in any given simulation). To isolate the effect of anisotropy, but avoid the physically unrealistic case of homogeneous media, we perturbed the permeability field with

$$k_{xx} = 1 + \delta, \tag{109}$$

where δ is a random number, uniformly distributed and of magnitude bounded by $|\delta| \leq 0.01$. The actual log-permeability (k_{xx}) field defined on a 64×64 fine grid is shown in Fig. 12.

The flow scenario is the same as the one described in the previous section: no-flow boundaries, with an injection well at the bottom-left corner and a producer at the top-right corner of the square domain. This is in fact a challenging test case that leads to the formation of boundary layers. The fine grid is a 64×64 grid, and we make use of several coarse meshes with unit aspect ratio: 4, 8, 16, and 32. As an illustration of the good behavior of the method, we show in Fig. 13 the pressure field computed with a finite volume method on the fine grid and the VMSMFE method for a value of the anisotropy ratio of $\alpha = 0.1$. The multiscale solution was computed on a 8×8 coarse grid and with a well length scale $N_l = 1/4$.

Figure 14 shows the velocity and pressure errors for different anisotropy ratios α and different choices of the coarse grid. The well length scale is set at a value $N_l = 1/4$ for all computations. The results reveal the very robust behavior of the proposed VMSMFE method with respect to anisotropy. For $\alpha = 1$ (isotropic), the method yields a very accurate solution for all coarse discretizations: $\varepsilon(\mathbf{u}) \approx 10^{-2}$ for all coarse grids, and $\varepsilon(p)$ decreases monotonically, as the coarse grid is

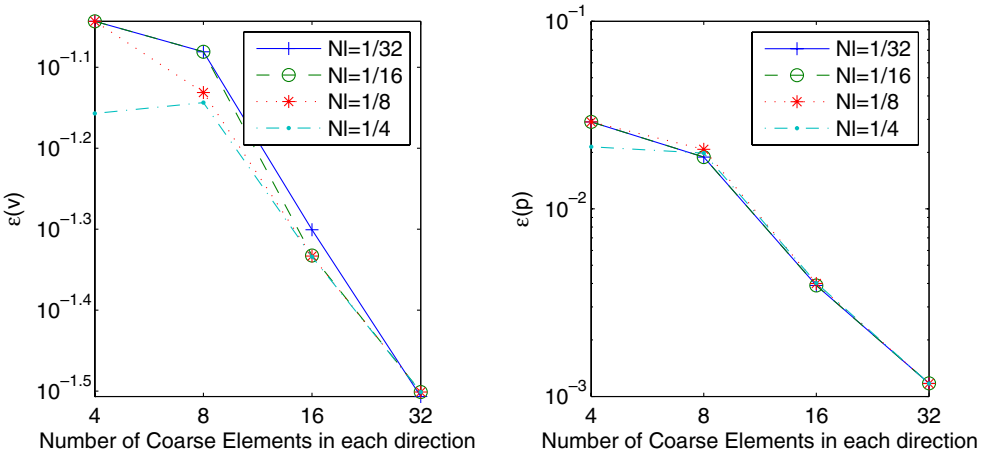

Fig. 7 Velocity (*left*) and pressure (*right*) errors for the isotropic correlation scenario

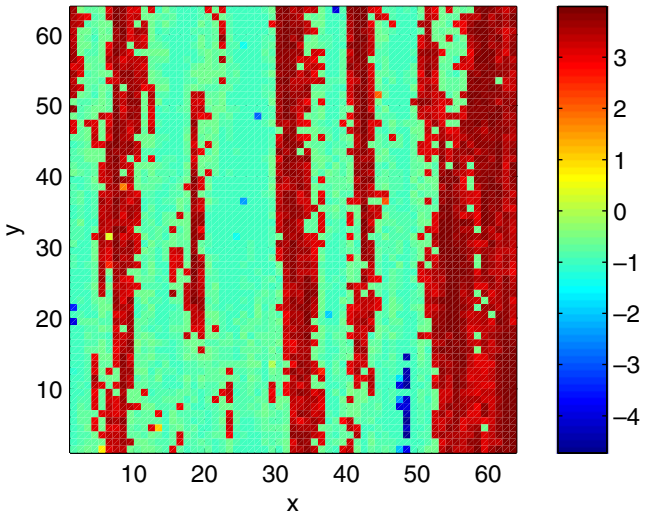

Fig. 8 Log-permeability field for the structure dominated by vertical channels

refined. Another indication of the robustness of the method is that the results for $\alpha = 10$ (resp. $\alpha = 100$) are virtually identical to those for $\alpha = 0.1$ (resp. $\alpha = 0.01$). Of course, increasing levels of anisotropy ($\alpha = 10, 100$) lead to larger velocity and pressure errors. However, the errors are still small, and they decrease with refinement of the coarse grid.

5.4 Simulations in realistic two-dimensional reservoirs

5.4.1 Highly heterogeneous, smoothly varying permeability

This test case is a two-dimensional problem with a highly heterogeneous isotropic permeability. The permeability field, shown in Fig. 15a, has large (but smooth) variations of 6 orders of magnitude. It is taken from the top layer of the 10th SPE comparative solution project [17]. The fine grid on which the permeability is defined consists of 60×220 gridblocks. All boundaries are no-flow boundaries. Flow is driven by an injection well at the center of the domain and four production wells, one at each corner (see Fig. 15a). Production wells are modeled as sinks over one fine gridblock – the corner gridblock. To respect symmetry, the production well is modeled as a source over four gridblocks on the fine grid. The location of fine-scale sources and sinks is independent of the choice of the coarse grid. Therefore, the wells may be placed at the center or at the boundary of a coarse element, depending on the coarse discretization.

The finite volume solution computed on the fine grid is shown in Fig. 15. Most of the pressure drop occurs at the low permeability region $20 < y < 40$. The contour plots of x- and y-flux clearly indicate flow focusing along the more permeable regions, bypassing the low-permeability areas. The velocity field displays, however, significant small-scale structure in response to the spatial permeability variations.

In Fig. 16, we show the solution (fine-scale pressure, x-flux and y-flux) obtained with the VMSMFE method on a coarse grid of 6×22 elements (each containing 10×10 fine blocks) and a well length scale of $N_l = 1/4$. Despite the severe heterogeneity and the rather aggressive 100-fold upgridding, the multiscale solution is remarkably accurate. The velocity error is $\varepsilon(\mathbf{u}) = 0.185$. Moreover, both the large and small scale flow patterns are captured with very high fidelity. It should be noted, however, that, although the average (coarse) pressure field is accurate, the reconstructed (fine) pressure presents slight oscillations at the interfaces between coarse elements.

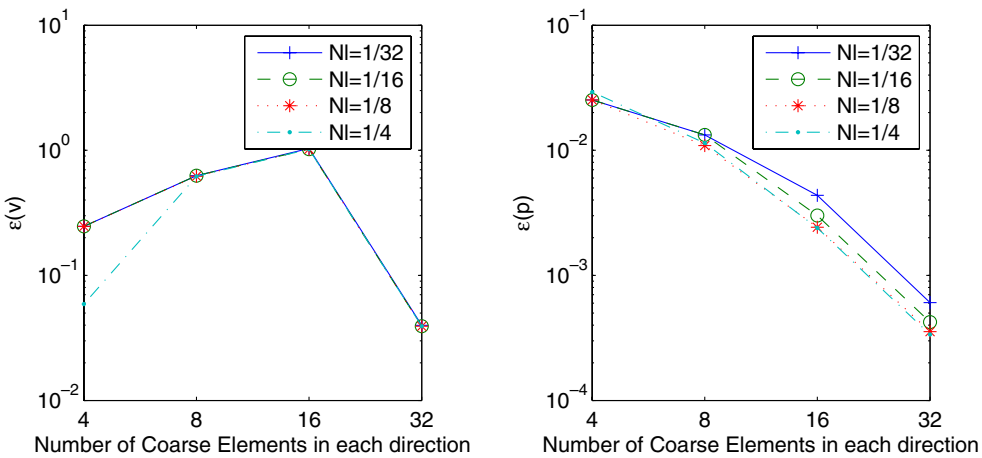

Fig. 9 Velocity (*left*) and pressure (*right*) errors for the scenario with vertical channels

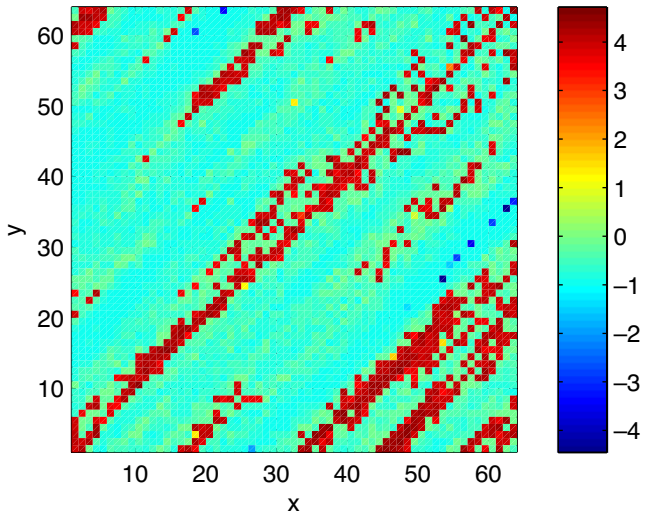

Fig. 10 Log-permeability field for the structure dominated by diagonal channels

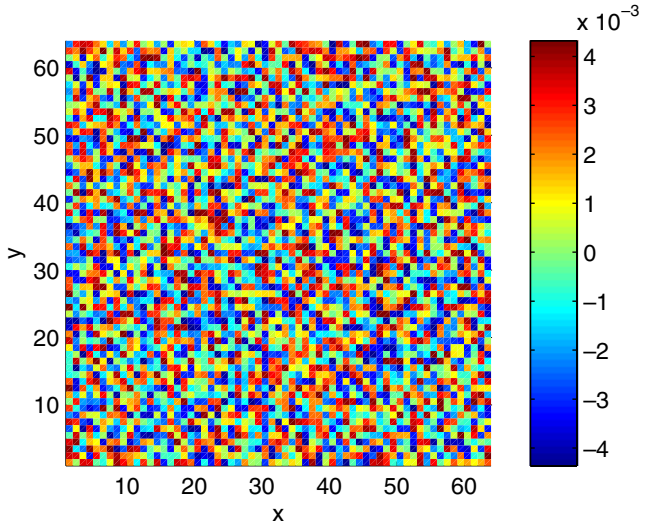

Fig. 12 Log-permeability (k_{xx}) field for the study of anisotropy

In Fig. 17, we show the velocity and pressure error of the VMS method for a fixed length scale $N_l = 1/4$ as a function of the coarse discretization into $N_x \times N_y$ elements, for all combinations of $N_x = \{6, 10, 30\}$ and $N_y = \{11, 22, 55, 110\}$. In this way, we test the robustness of the method with respect to not only coarseness of the (coarse) grid, but also to (coarse) grid aspect ratio. We make the following observations:

- The method displays very good behavior even for aggressive upgridding. As expected, the error is smaller for discretizations with aspect ratio close to unity (6×22, 10×55, and 30×110 grids), and it decreases with refinement of the coarse grid.
- The pressure error is very small, between 10^{-3} and 10^{-2} in most cases. Pressure errors are larger, however, for grids with $N_y = 11$. These grids have coarse elements with 20 fine gridblocks in the y-direction – approximately the extent of the low-permeability zone.
- The velocity error is larger for grids with a large aspect ratio (notably, for the 6×110 coarse grid).

5.4.2 Highly heterogeneous, channelized permeability

This test case is a challenging two-dimensional problem with a highly heterogeneous, but now rough (channelized) permeability field (see Fig. 18a). It is a synthetic model of a fluvial reservoir, taken from Layer 59 of the 10th SPE comparative solution project. The fine grid, boundary conditions, and well locations are the same as in the previous example.

In Fig. 18, we plot the pressure and fluxes from a fine-grid finite volume solution. The most salient feature is the pronounced focusing of flow along the high-

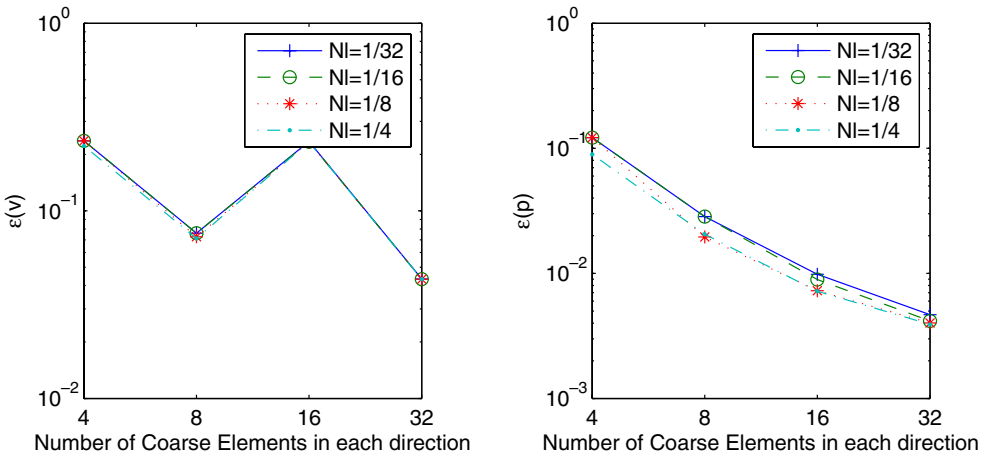

Fig. 11 Velocity (*left*) and pressure (*right*) errors for the scenario with diagonal channels

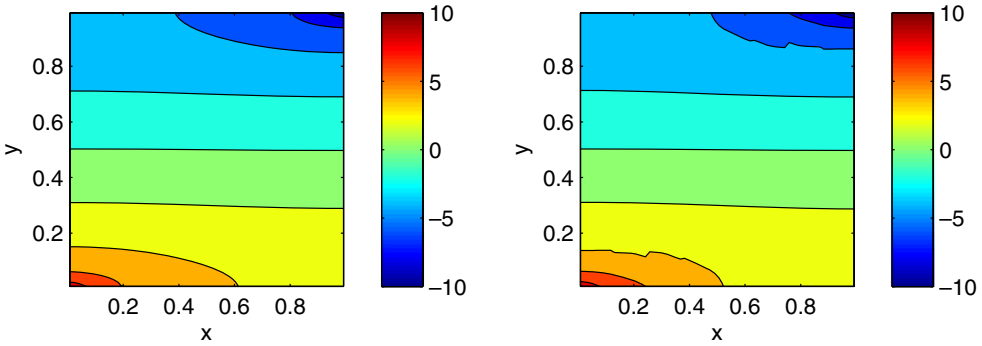

Fig. 13 Pressure field for the anisotropic permeability field ($\alpha = 0.1$). *Left* fine-scale finite volume solution. *Right* variational multiscale solution on a 8×8 grid (8×8 upgridding)

permeability channels, leading to very high velocities (in both x- and y-directions) over very narrow regions of the domain. This is also true near the injection and production wells.

The VMS solution is shown in Fig. 19. It was computed, as before, on a coarse grid of 6×22 elements, each containing 10×10 fine blocks, using a well length scale of $N_l = 1/4$. The method is able to capture the high-velocity regions very accurately, although they have a long range in the streamwise direction and a very short range in the spanwise direction. The global flow pattern is reproduced accurately as well. This is evidenced by the small mean velocity error of $\varepsilon(\mathbf{u}) = 0.330$. Clearly, an essential ingredient of the proposed method is its ability to account for subgrid variability at the element interfaces. Once again, the multiscale pressure solution agrees well with the fine-grid finite volume solution on an average sense, but presents mild discrepancies after the fine-scale reconstruction step, including spurious local maxima at coarse element interfaces.

The mean velocity and pressure errors of the VMS method for a fixed well length scale $N_l = 1/4$ and for various coarse grids are shown in Fig. 20. As in the previous example, the bar plot displays a valley (minima) for discretizations with grid aspect ratio close to unity (6×22, 10×55, and 30×110) and hills (maxima) for discretizations with large aspect ratios (30×11 and 6×110).

Given the large values of the velocity error $\varepsilon(\mathbf{u})$, we investigate the applicability of the VMS method for the accurate simulation of transport problems. We simulate the transport of a passive tracer, described by the advection equation, using a single-point upstream discretization, and an explicit forward Euler time stepping [8]. The velocity field is fixed from the solution to the pressure equation. We use the reconstructed fine-scale fluxes obtained with the VMS method on various coarse grids. The computed concentration field on a number of different coarse grids is shown in Fig. 21. The concentration fields are of very high quality, even for the coarse grids on which the fluxes display large errors (that is, the 30×22 and 30×55 grids).

The VMS method is also able to capture the behavior of the breakthrough curves of the passive tracer at the production wells. As shown in Fig. 22, the breakthrough curves computed with the 6×22 and 30×55 grids show very mild inaccuracies. The results for the 30×22

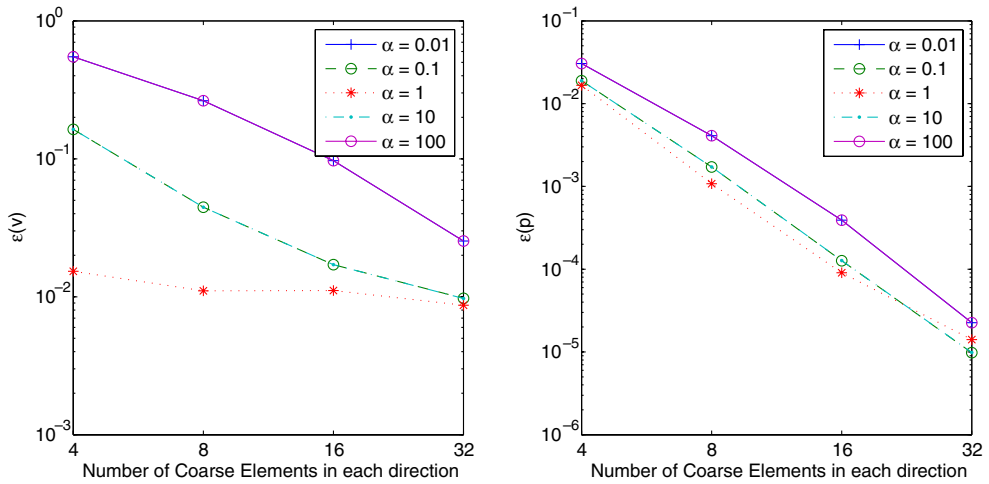

Fig. 14 Velocity (*left*) and pressure (*right*) errors for the anisotropic permeability field

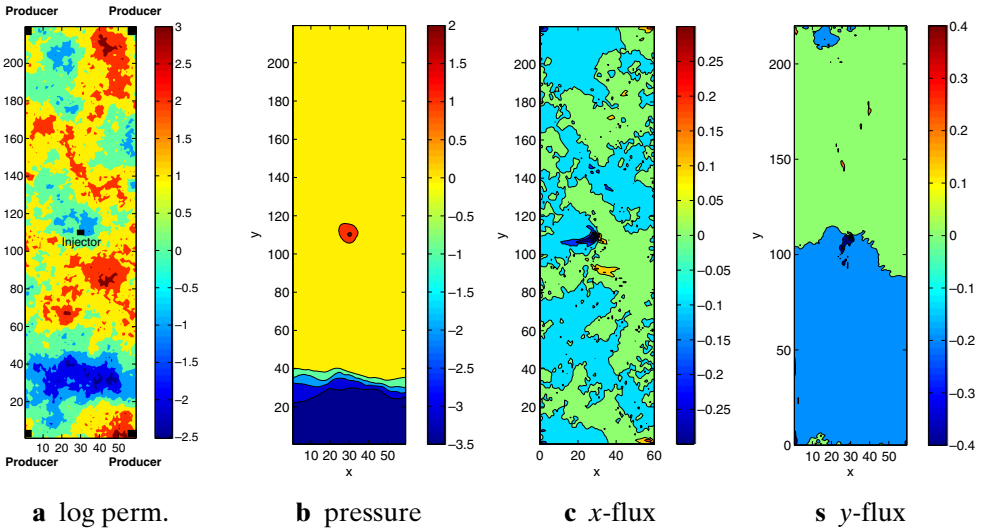

Fig. 15 Smooth permeability field. Finite volume solution on the fine 60×220 grid

a log perm. **b** pressure **c** x-flux **s** y-flux

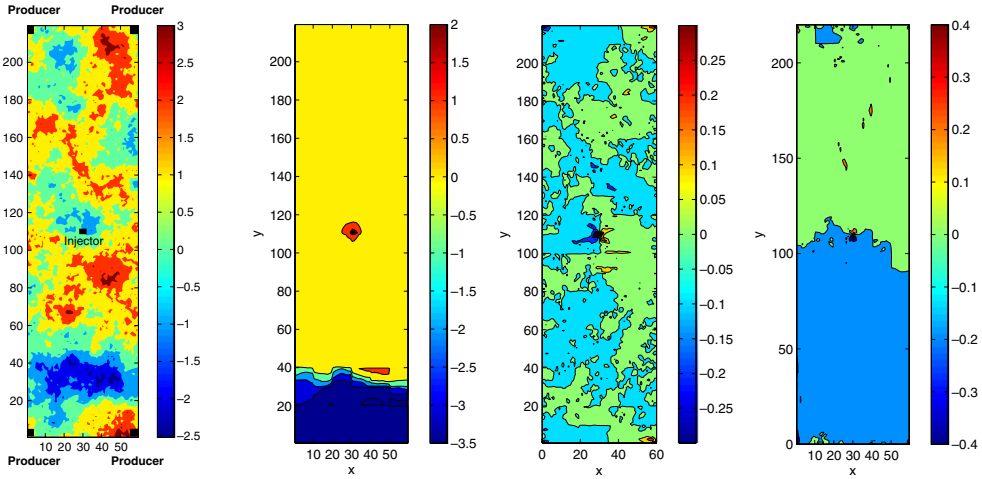

Fig. 16 Smooth permeability field. VMS solution on a 6×22 grid (10×10 upgridding) with well length scale $N_l = 1/4$

a log perm. **b** pressure **c** x-flux **c** y-flux

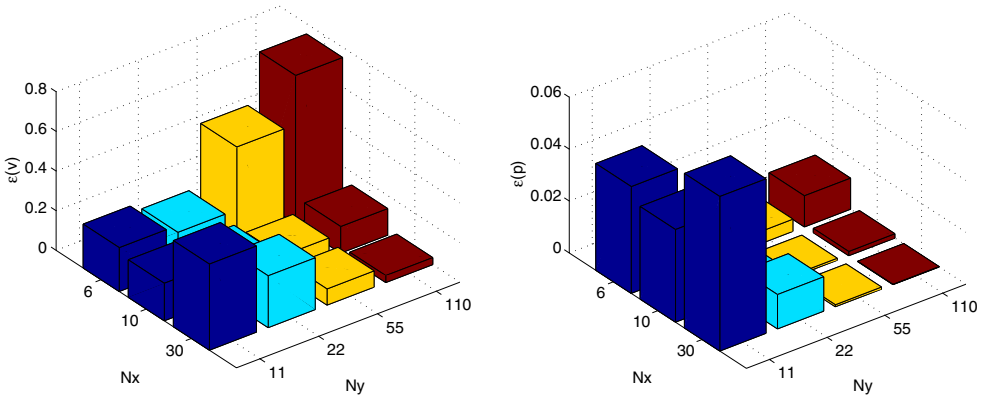

Fig. 17 Smooth permeability field. Velocity and pressure errors for different coarse discretizations

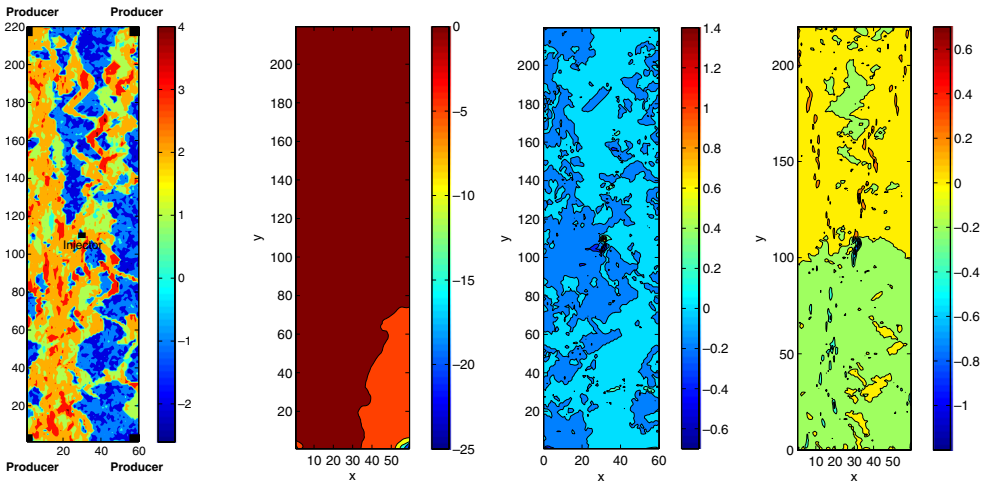

Fig. 18 Channelized permeability field. Finite volume solution on the fine 60×220 grid

a log perm. **b** pressure **c** x-flux **d** y-flux

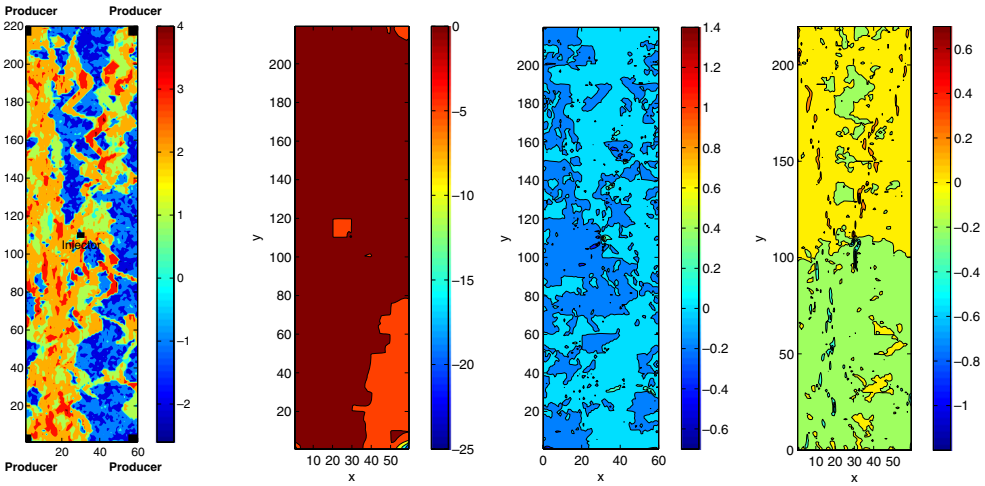

Fig. 19 Channelized permeability field. VMS solution on a 6×22 grid (10×10 upgridding) with well length scale $N_l = 1/4$

a log perm. **b** pressure **c** x-flux **d** y-flux

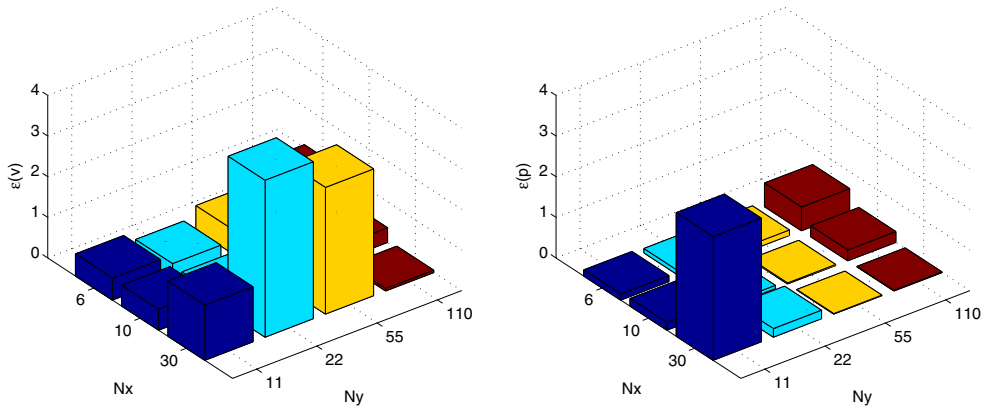

Fig. 20 Channelized permeability field. Velocity and pressure errors for different coarse discretizations

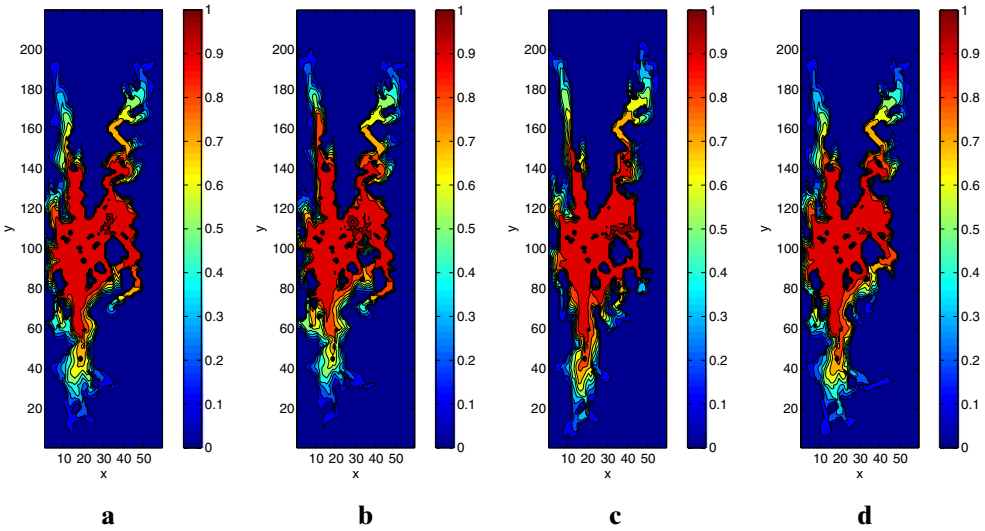

Fig. 21 Concentration maps at breakthrough with fluxes obtained by **a** finite volume method on the fine 60×220 grid; **b** VMS on a 6×22 grid; **c** VMS on a 30×22 grid; **d** VMS on a 30×55 grid

grid are less accurate, but still far better than the velocity error of $\varepsilon(\mathbf{u}) \approx 4$ would suggest. These results show that the VMS method is applicable for accurate simulation of transport problems and that the measure given by the global velocity error $\varepsilon(\mathbf{u})$ may be overly pessimistic.

5.4.3 All layers

We complete our analysis of the performance of the proposed VMS method by simulating the same injection–production scenario for all layers of the 10th SPE comparative solution project, which includes

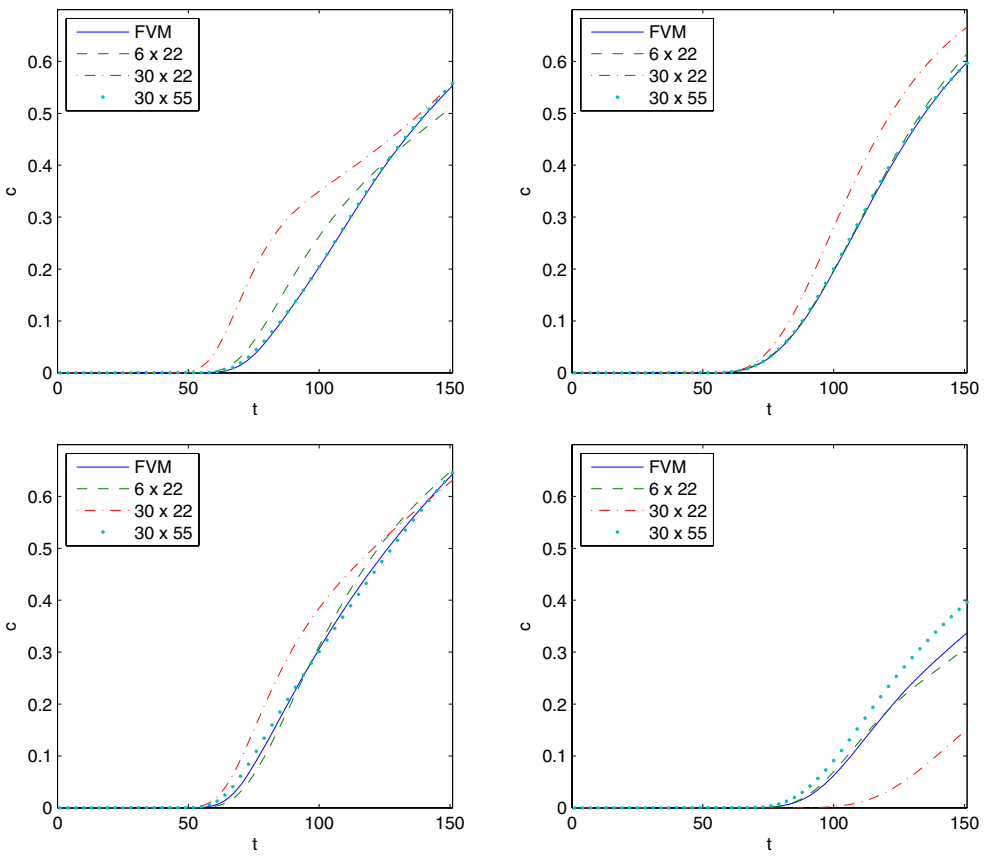

Fig. 22 Breakthrough curves of the passive tracer at each of the production wells, computed using fine-scale fluxes from different coarse-grid discretizations. *Clockwise, from top-left*: Top-left well; Top-right well; Bottom-right well; Bottom-left well

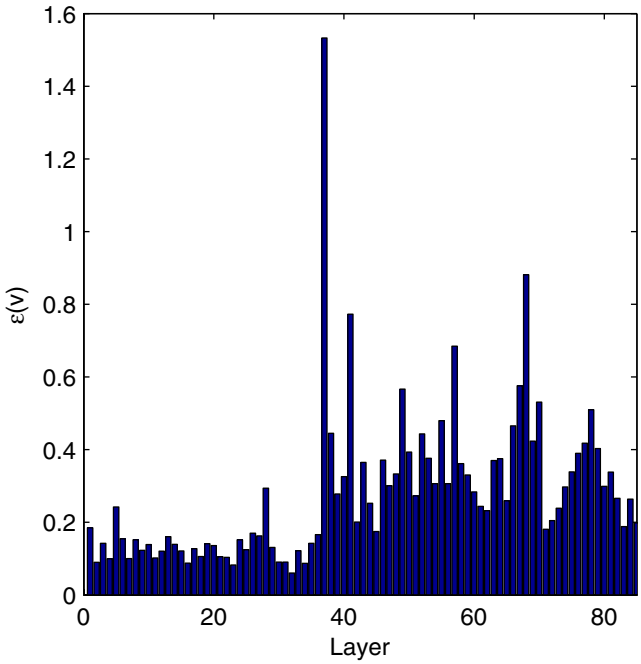

Fig. 23 All layers of the 10th SPE comparative solution project. Velocity error

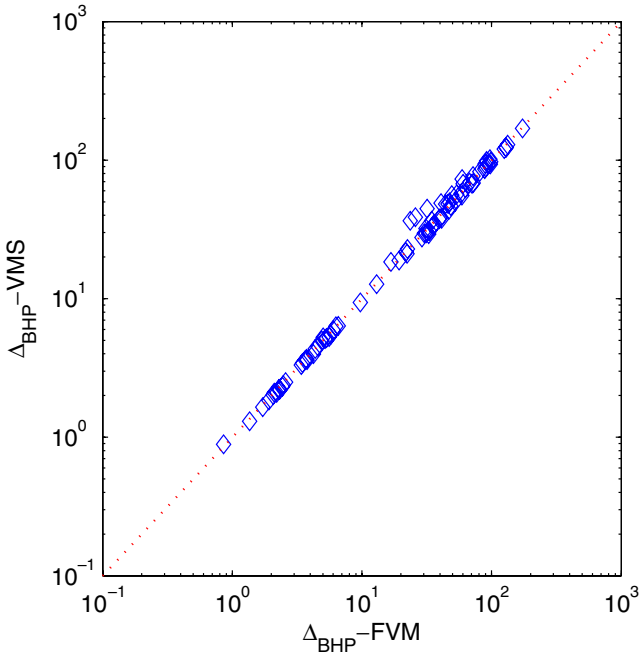

Fig. 25 Comparison of Δ_{BHP} between the reference finite volume solution and the VMS solution with 100-fold upgridding for all layers of the 10th SPE comparative solution project

the two previous test cases and 83 other layers. The first 35 layers correspond to the Tarbert formation and display large, but smooth, variations in permeability. The last 50 layers correspond to the Upper Ness formation and are characterized by a channelized permeability field.

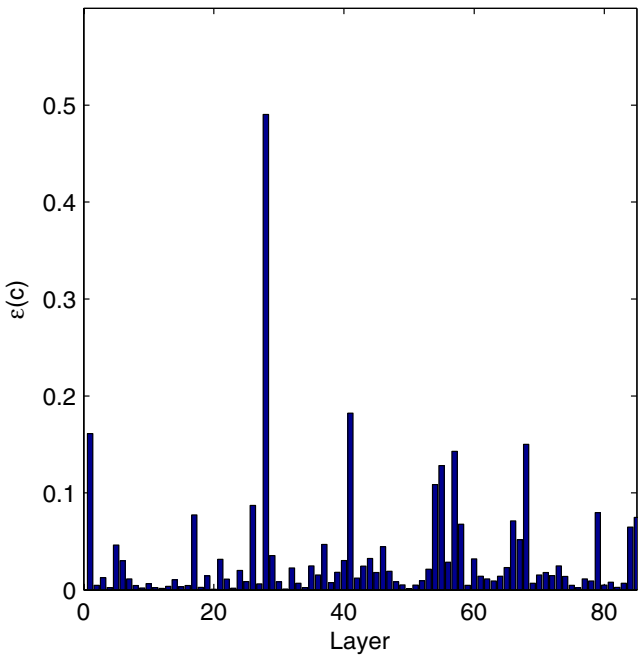

Fig. 24 All layers of the 10th SPE comparative solution project. Concentration error

Fine-scale velocity Finite volume solutions are computed on a fine grid of 60×220 gridblocks, on which the permeability field is defined. In Fig. 23, we plot the velocity error of the VMSMFE solution for each layer. The multiscale solution was computed using a well length scale of $N_l = 1/4$ and a 6×22 coarse grid (10×10 upgridding). It is apparent that the errors are consistently lower for the first 35 layers, for which the permeability field is smoother.

Simulation of transport The computed velocity error takes large values, in the range 0.3–1.0, for the layers in the highly channelized formation. As shown in the previous subsection, however, this large velocity error does not necessarily mean that the VMS method fails to give accurate solutions to transport problems. To illustrate this, we simulate the transport of a passive tracer using the reconstructed fine-scale fluxes from the VMS solution on a 6×22 grid and compare the solution to a reference finite volume solution on the fine grid. We employ a simple measure of the mean concentration error (at breakthrough in the first production well) computed in the following manner:

$$\varepsilon(c) = \frac{\|\mathsf{c} - \mathsf{c}^{\mathrm{ref}}\|^2}{\|\mathsf{c}^{\mathrm{ref}}\|^2}, \tag{110}$$

where c and $\mathsf{c}^{\mathrm{ref}}$ are array vectors that contain the average tracer concentration in each fine element (multi-

scale solution and reference finite volume solution, respectively) and $\|\cdot\|$ is the usual discrete l^2 norm.

In Fig. 24, we plot the concentration error at breakthrough for each layer. Clearly, the error remains small, even for the challenging layers corresponding to the Upper Ness formation. The mean concentration error is $\langle\varepsilon(c)\rangle \approx 0.033$, almost an order of magnitude smaller than the average velocity error, $\langle\varepsilon(\mathbf{u})\rangle \approx 0.28$. These results indicate that the measure given by the velocity error is too stringent and not entirely representative of the quality of the flow solution.

Well pressures In practice, well rates are dependent on the difference between the well pressure and the gridblock pressure. Therefore, it is very important that the fine-scale pressure be of high quality. In this study, we measure the quality of the fine-scale pressure solution by computing a weighted pressure difference between injectors and producers. More precisely, we compute the following quantity:

$$\Delta_{\mathrm{BHP}} := \sum_{j=1}^{N_w} Q_j \mathsf{p}_j, \tag{111}$$

where Q_j is the well rate (positive for injectors, negative for producers) and p_j is the well fine-scale gridblock pressure. For each layer, we compare the computed quantity Δ_{BHP} from a fine-scale finite volume solution and the VMSMFE solution on a 6×22 grid (100-fold upgridding) with $N_l = 1/4$. This comparison is shown in Fig. 25. For the entire range of values, Δ_{BHP} from the VMS solution is remarkably accurate – if the VMS solution were exact, the graph would show a perfect 1 : 1 correlation. This is an essential property for the practical use of the proposed VMS method in reservoir simulation.

6 Conclusions and future work

The numerical simulations of the previous section demonstrate that the VMS mixed finite element method provides highly accurate solutions to flow scenarios with challenging permeability fields and concentrated fine-scale source terms. In the spirit of many other multiscale methods, this is accomplished through the solution of a global coarse-grid problem that incorporates (rigorously, in a variational setting) the effect of the subgrid scales computed locally. The method is an extension of the numerical subgrid upscaling technique proposed in [4] and, as we show here, has a clear connection with the multiscale mixed finite element method [27]. The key ingredients of our method are:

1. A weak localization assumption of the subgrid problems that allows for subgrid communication across element interfaces.
2. A decomposition of fine-scale source terms into coarse and deviatoric components and the definition of multiscale "well" basis functions.

The method is locally conservative, flux-continuous, and employs a low-order mixed finite element approximation at both scales. The method, as presented here, is amenable to a number of extensions, such as:

1. Introducing a Peaceman-type well model for practical use of the method in reservoir simulation.
2. Coupling with the transport equation and extending it to the nonlinear regime (non-unit mobility ratio and multiphase flow).
3. Incorporating global information in the definition of the local subgrid problems, in the spirit of the coupled local–global upscaling approach [15, 18].

Acknowledgements We thank Vegard Kippe for providing the permeability fields used in Section 5.2. The second author was partly supported by an MIT-Total graduate fellowship.

References

1. Aarnes, J.E.: On the use of a mixed multiscale finite element method for greater flexibility and increased speed or improved accuracy in reservoir simulation. Multiscale Model. Simul. **2**(3), 421–439 (2004)
2. Aarnes, J.E., Kippe, V., Lie, K.A.: Mixed multiscale finite elements and streamline methods for reservoir simulation of large geomodels. Adv. Water Resour. **28**, 257–271 (2005)
3. Arbogast, T.: Numerical subgrid upscaling of two-phase flow in porous media. In: Chen, Z., Ewing, R.E., Shi, Z.C. (eds.) Numerical Treatment of Multiphase Flow in Porous Media. Lecture Notes in Physics, vol. 552, pp. 35–49. Springer (2000)
4. Arbogast, T.: Implementation of a locally conservative numerical subgrid upscaling scheme for two-phase Darcy flow. Comput. Geosci. **6**(3–4), 453–481 (2002)
5. Arbogast, T.: Analysis of a two-scale, locally conservative subgrid upscaling for elliptic problems. SIAM J. Numer. Anal. **42**(2), 576–598 (2004)
6. Arbogast, T., Boyd, K.J.: Subgrid upscaling and mixed multiscale finite elements. SIAM J. Numer. Anal. **44**(3), 1150–1171 (2006)
7. Arbogast, T., Bryant, S.L.: A two-scale numerical subgrid technique for waterflood simulation. Soc. Pet. Eng. J. **7**(4), 446–456 (2002)
8. Aziz, K., Settari, A.: Petroleum Reservoir Simulation. Elsevier, London (1979)
9. Babuška, I.: The finite element method with Lagrangian multipliers. Numer. Math. **20**, 179–192 (1973)
10. Babuška, I., Osborn, J.E.: Generalized finite element methods: their performance and their relation to mixed methods. SIAM J. Numer. Anal. **20**(3), 510–536 (1983)

11. Babuška, I., Caloz, G., Osborn, J.E.: Special finite element methods for a class of second order elliptic problems with rough coefficients. SIAM J. Numer. Anal. **31**(4), 945–981 (1994)
12. Brezzi, F.: On the existence, uniqueness and approximation of saddle point problems arising from Lagrange multipliers. RAIRO Anal. Numér. **8**, 129–151 (1974)
13. Brezzi, F., Fortin, M.: Mixed and Hybrid Finite Element Methods, Springer Series in Computational Mathematics, vol. 15. Springer-Verlag, New York (1991)
14. Brezzi, F., Douglas, Jr., J., Marini, L.D.: Two families of mixed finite elements for second order elliptic problems. Numer. Math. **47**, 217–235 (1985)
15. Chen, Y., Durlofsky, L.J., Gerritsen, M., Wen, X.H.: A coupled local–global upscaling approach for simulating flow in highly heterogeneous formations. Adv. Water Resour. **26**(10), 1041–1060 (2003)
16. Chen, Z., Hou, T.Y.: A mixed multiscale finite element method for elliptic problems with oscillating coefficients. Math. Comp. **72**(242), 541–576 (2002)
17. Christie, M.A., Blunt, M.J.: Tenth SPE comparative solution project: a comparison of upscaling techniques. SPE Reserv. Eval. Eng. **4**(4), 308–317 (2001). www.spe.org/csp
18. Durlofsky, L.J., Efendiev, Y., Ginting, V.: An adaptive local-global multiscale finite volume element method for two-phase flow simulations. Adv. Water Resour. **30**, 576–588 (2007)
19. Efendiev, Y.R., Hou, T.Y., Wu, X.H.: Convergence of a nonconforming multiscale finite element method. SIAM J. Numer. Anal. **37**(3), 888–910 (2000)
20. Hou, T.Y., Wu, X.H.: A multiscale finite element method for elliptic problems in composite materials and porous media. J. Comput. Phys. **134**, 169–189 (1997)
21. Hou, T.Y., Wu, X.H., Cai, Z.: Convergence of a multiscale finite element method for elliptic problems with rapidly oscillating coefficients. Math. Comp. **68**(227), 913–943 (1999)
22. Hughes, T.J.R.: Multiscale phenomena: green's functions, the Dirichlet-to-Neumann formulation, subgrid scale models, bubbles and the origins of stabilized methods. Comput. Methods Appl. Mech. Eng. **127**, 387–401 (1995)
23. Hughes, T.J.R., Feijóo, G.R., Mazzei, L., Quincy, J.B.: The variational multiscale method – a paradigm for computational mechanics. Comput. Methods Appl. Mech. Eng. **166**, 3–24 (1998)
24. Jenny, P., Lee, S.H., Tchelepi, H.A.: Multi-scale finite-volume method for elliptic problems in subsurface flow simulation. J. Comput. Phys. **187**(1), 47–67 (2003)
25. Jenny, P., Lee, S.H., Tchelepi, H.A.: Adaptive multiscale finite-volume method for multiphase flow and transport in porous media. Multiscale Model. Simul. **3**(1), 50–64 (2004)
26. Juanes, R.: A variational multiscale method for the simulation of porous media flow in highly heterogeneous formations. In: Computational Methods in Water Resources XVI, Paper 249. Copenhagen, Denmark (2006), http://proceedings.cmwr-xvi.org
27. Kippe, V., Aarnes, J.E., Lie, K.A.: A comparison of multiscale methods for elliptic problems in porous media flow. Comput Geosci, Special Issue on Multiscale Methods for Flow and Transport in Heterogeneous Porous Media (2008). doi:10.1007/s10596-007-9074-6
28. Lee, S.H., Wolfsteiner, C., Tchelepi, H.A.: Multiscale finite-volume formulation for multiphase flow in porous media: black oil formulation of compressible, three phase flow with gravity. Comput Geosci, Special Issue on Multiscale Methods for Flow and Transport in Heterogeneous Porous Media (2008). doi:10.1007/s10596-007-9069-3
29. Lunati, I., Jenny, P.: Treating highly anisotropic subsurface flow with the multiscale finite-volume method. Multiscale Model. Simul. **6**(1), 308–318 (2007)
30. Peaceman, D.W.: Interpretation of well-block pressures in numerical reservoir simulation. In: SPE Annual Technical Conference and Exhibition. Denver, CO (SPE 6893) (1977)
31. Raviart, P.A., Thomas, J.M.: A mixed finite element method for second order elliptic problems. In: Galligani, I., Magenes, E. (eds.) Mathematical Aspects of the Finite Element Method. Lecture Notes in Mathematics, vol. 606, pp. 292–315. Springer-Verlag, New York (1977)
32. Russell, T.F., Wheeler, M.F.: Finite element and finite difference methods for continuous flows in porous media. In: Ewing, R.E. (ed.) The Mathematics of Reservoir Simulation, pp 35–106. SIAM Philadelphia, PA (1983)
33. Weiser, A., Wheeler, M.F.: On convergence of block-centered finite differences for elliptic problems. SIAM J. Numer. Anal. **25**(2), 351–375 (1988)
34. Wolfsteiner, C., Lee, S.H., Tchelepi, H.A.: Well modeling in the multiscale finite volume method for subsurface flow simulation. Multiscale Model. Simul. **5**(3), 900–917 (2006)